Assessment of OLCI-A and OLCI-B radiometric data products across European seas

Giuseppe Zibordi [a,*], Ewa Kwiatkowska [b], Frédéric Mélin [a], Marco Talone [c], Ilaria Cazzaniga [a], David Dessailly [b], Juan Ignacio Gossn [b]

[a] *Joint Research Centre of the European Commission, Ispra, Italy*
[b] *EUMETSAT, Remote Sensing and Products Division, Darmstadt, Germany*
[c] *Barcelona Expert Centre and Institute of Marine Sciences (ICM-CSIC), Barcelona, Spain*

ARTICLE INFO

Editor: Menghua Wang

ABSTRACT

The Ocean and Land Color Instruments (OLCI) operated onboard the Copernicus Sentinel-3 satellites are providing globally distributed Ocean Color Radiometry (OCR) data products of relevance for environmental and climate applications. This work summarizes results on the assessment of fundamental OCR data from the Operational Baseline 3 Collection OL_L2M.003.01 of OLCI-A and OLCI-B onboard Sentinel-3A and Sentinel-3B, respectively. Evaluated products are the satellite derived normalized water-leaving radiance $L_{WN}(\lambda)$, aerosol optical depth at 865 nm $\tau_a(865)$ and Ångström exponent α determined in the near-infrared spectral region. The analyses were performed relying on *in situ* reference data from the Ocean Color component of the Aerosol Robotic Network (AERONET-OC) from sites representative of diverse water types. The comparison of OLCI-A and OLCI-B with AERONET-OC $L_{WN}(\lambda)$ for oligotrophic/mesotrophic waters shows cross-mission consistent spectral median percent differences (*i.e.*, biases) varying within ±6% at the blue-green center-wavelengths. The analysis of data from regions characterized by optically complex waters, however, displays systematic negative biases for both OLCI-A and OLCI-B further increasing for waters dominated by chromophoric dissolved organic matter, thus suggesting a dependence of the atmospheric correction on water type. The direct inter-comparison of OLCI-B and OLCI-A $L_{WN}(\lambda)$ from the *Tandem Phase* characterized by Sentinel-3B and Sentinel-3A flying 30 s apart on the same orbit, shows spectral median percent differences lower than ±1% in the 412–560 nm interval, of approximately +5% at 620 and 665 nm, and −7% at 400 nm. However, outside the *Tandem Phase*, the inter-comparison of OLCI-B and OLCI-A data products indicates large and systematic differences explained by a notable dependence on the viewing angle. The evaluation of $\tau_a(865)$ and α across different geographic regions exhibits overestimated values between +48 and +79% for the former and underestimated values between −28% and −41% for the latter. A complementary evaluation of OCR data products from the Visible Infrared Imager Radiometer Suite on board the Suomi National Polar-orbiting Partnership (VIIRS-S), proposed as a further in-direct term of reference for OLCI-A and OLCI-B data, shows large underestimates of $L_{WN}(\lambda)$ with respect to the *in situ* reference data in the various water types at 410 nm. Nevertheless, opposite to OLCI-A and OLCI-B data products, absolute differences between VIIRS-S and *in situ* reference data do not reveal any large or systematic dependence on water type and satellite viewing angle. Overall results suggest the need for further developing the OLCI-A and OLCI-B atmospheric correction, possibly improving the capability to identify aerosol types and to model scattering processes.

1. Introduction

Accurate, globally distributed, sustained and accessible data of climate variables are essential to address planetary climate issues. This fundamental need steered the creation of the Global Climate Observing System (GCOS) to ensure access to key physical, chemical and biological observations with the necessary accuracy (World Meteorological Organization (WMO), 2011). Ocean Colour Radiometry (OCR) and its derived products (*e.g.*, chlorophyll-*a* concentration (Chl*a*), a proxy for phytoplankton biomass) are included among the GCOS Essential Climate

Variables (ECV) because of their fundamental relevance in assessing the impact of climate change on marine ecosystems (Behrenfeld et al., 2006) and, at large, to quantify the oceans role on the global carbon cycle (Lohrenz and Cai, 2006). These fundamental applications of OCR have been the rationale for satellite ocean color sensors designed and operated by various space agencies. Following the precursor Coastal Zone Color Scanner (CZCS) working from 1978 till 1986, a number of satellite ocean color sensors have been successfully operated since 1997. Those ensuring global coverage and supported by a wide data distribution, are of paramount importance and include the Sea-viewing Wide Field-of-view sensor (SeaWiFS: McClain, 2009), the Moderate-resolution Imaging Spectroradiometer (MODIS: Esaias et al., 1998), the Medium Resolution Imaging Spectrometer (MERIS: Bezy et al., 2000), the Visible Infrared Imaging Radiometer Suite (VIIRS: Goldberg et al., 2013; Schueler et al., 2002) and recently the Ocean and Land Color Instrument (OLCI: Donlon et al., 2012).

Copernicus Sentinel-3 missions, including the current Sentinel-3A launched on February 16, 2016, and Sentinel-3B launched on April 25, 2018, together with Sentinel-3C and Sentinel-3D planned beyond 2023, will warrant continuous and sustained support to OCR through OLCI data for two decades (Donlon et al., 2012). This unprecedented effort to generate globally distributed time-series of satellite data from a suite of successive identical missions is expected to have foremost relevance for climate investigations. In fact, the adoption of identical space technology and data reduction will minimize the potential for biases commonly affecting data products from independent missions, thus increasing the capability to produce data records fulfilling uncertainty and temporal stability requirements for climate applications (Ohring et al., 2005).

Achieving uncertainty and temporal stability requirements, nevertheless, implies applying robust calibration and validation strategies allowing *i.* to trace responsivity changes of satellite sensors during their lifecycle (*e.g.*, Eplee et al., 2012), *ii.* to determine mission specific System Vicarious Calibration (SVC) adjustment factors, so called *g*-factors, to minimize biases due to limitations affecting sensor pre-launch calibration and data processing (*e.g.*, Zibordi et al., 2015), and finally *iii.* to continuously assess the fitness-for-purpose of data products across the variety of environmental conditions characterizing the world oceans.

The core data product of any satellite ocean colour mission is the spectral water-leaving radiance L_W (and the derived normalized water-leaving radiance L_{WN}), which is the radiance emerging from below the sea surface quantified from the at-the-sensor radiance (IOCCG, 2010). This is obtained through the atmospheric correction process that removes the perturbing effects of atmospheric scattering and absorption responsible for most of the at-the-sensor signal. Core OCR data products are commonly assessed using *in situ* reference measurements traceable to the International System of Units (SI), for which uncertainties should be assigned.

The objective of this work is to investigate the accuracy of Sentinel-3A and Sentinel-3B OLCI (hereafter referred to as OLCI-A and OLCI-B,

respectively) OCR data products from the Operational Baseline 3 Collection OL_L2M.003.01, generated by the European Organization for the Exploitation of Meteorological Satellites (EUMETSAT) with the processor IPF-OL-2 version 07.01 released in April 2021. This assessment exploits *in situ* reference data from the Ocean Color component of the Aerosol Robotic Network (AERONET-OC) by considering measurement sites representative of diverse water types and observation conditions so that results are comprehensive and reflect different marine environments and regions. Finally, aiming at providing a further term of reference for OLCI-A and OLCI-B data products, an equivalent assessment is proposed and discussed for OCR data products from the Visible Infrared Imaging Radiometer Suite on board the Suomi National Polar-orbiting Partnership (VIIRS-S).

2. Data and methods

Brief descriptions of *i.* the OCR data products evaluated in this work, *ii.* the *in situ* reference data applied for their assessment and *iii.* the methods supporting the analyses proposed, are provided in the following sub-sections. Table 1 summarizes the various data products, the time frame for which they exist or were considered, and their processing level and version.

2.1. OLCI data products

OLCI (either OLCI-A and OLCI-B) are push-brooms imaging spectrometers composed of five cameras whose ensemble is tilted toward west to limit the impact of sun-glint. The primary quantity assessed in this work is the *spectral normalized water-leaving radiance* $L_{WN}^{OLCI}(\lambda)$ determined at the center-wavelengths λ from the *water reflectance* $\rho_w^{OLCI}(\lambda)$ Level-2 Reduced-Resolution (1.2-km) data products from the Operational Baseline 3 Collection OL_L2M.003.01 (EUMETSAT, 2021a), relevant for global applications.

OLCI Level-2 pre- and main-processing are hereafter briefly summarized. In the pre-processing stage, each OLCI Level-1 pixel radiance is converted to reflectance, classified (which includes cloud flagging) and corrected for atmospheric ozone, water vapor, oxygen and NO_2 absorption (Fischer et al., 2010). In the following main-processing stage, the atmospheric correction is applied to each pixel classified as water. The so called *standard* and *alternative* atmospheric corrections are performed in parallel (EUMETSAT, 2021a, 2021b). The water reflectance products relevant for this work are those from the standard atmospheric correction. In fact, the water reflectance from the alternative atmospheric correction, which is specific to complex waters, is not included among the data distributed.

The standard processing includes a number of successive steps: *i.* the correction for glint and white cap perturbations (Lavander and Kay, 2010; EUMETSAT, 2021a); *ii.* the application of pressure-related corrections for Rayleigh scattering; *iii.* the correction for spectral differences (*i.e.*, smile correction) across OLCI cameras (Vincent and Muguet,

Table 1

Summary of the satellite and *in situ* data applied in the following analysis (see text for acronyms).

In situ site / Satellite sensor	Time frame	Level	Processing version	Source
AAOT	04-10-2017 15-09-2020	2.0	Version-3	NASA/AERONET-OC
CPL	02-04-2019 15-04-2021	1.5	Version-3	NASA/AERONET-OC
GDLT[1]	04-05-2018 11-09-2020	2.0	Version-3	NASA/AERONET-OC
GLR	16-03-2018 06-08-2019	2.0	Version-3	NASA/AERONET-OC
GLT	10-11-2018 21-10-2020	2.0	Version-3	NASA/AERONET-OC
HLT[1]	18-06-2019 04-09-2019	2.0	Version-3	NASA/AERONET-OC
ILT[2]	24-07-2018 20-07-2020	2.0	Version-3	NASA/AERONET-OC
ST7	27-08-2019 15-03-2021	1.5	Version-3	NASA/AERONET-OC
OLCI-A	26-04-2016 15-03-2021	2.0	OL_L2M.003.01	EUMETSAT
OLCI-B	15-05-2018 15-03-2021	2.0	OL_L2M.003.01	EUMETSAT
VIIRS-S	06-01-2012 30-06-2020	2.0	R2018	NASA/OB.DAAC

[1] Spring-summer deployments.

[2] Occasional deployments.

2010); *iv.* the application of the SVC *g*-factors to each spectral band (Mazeran and Ruescas, 2021); and finally *v.* the removal of potential contributions of water reflectance in the near-infrared spectral bands through the Bright Pixel Correction (BPC) (Mazeran et al., 2021).

The above steps set the stage for the main atmospheric correction process removing the contributions of molecular scattering and of aerosol scattering/absorption (where the aerosol effects are the main unknown in the overall correction process). Following the approach detailed in Antoine and Morel (1999), an aerosol model is selected by exploiting the data at the 779 and 865 nm center-wavelengths, and assuming that the signal in the near-infrared is exclusively due to the atmosphere. Thirteen maritime, coastal and rural aerosol mixtures with continental and stratospheric background, as defined by Shettle and Fenn (1979), are available for the selection process. Additional eighteen desert dust aerosol models of large, medium and small particles, as defined by Moulin et al. (2001) are also accessible and can be identified through a specific test applied to the 510 nm center-wavelength data (Nobileau and Antoine, 2005). When two bounding aerosol models are determined for the pixel, the water reflectance is then quantified by removing the atmospheric contribution throughout the visible spectrum for both Rayleigh and those aerosols (Antoine, 2010). It is recalled that the OLCI water reflectance data product (*i.e.*, $\rho_w^{OLCI}(\lambda)$) is normalized to the illumination conditions determined by the sun at the zenith and at the mean distance from the earth, but it is not corrected for bidirectional effects.

Major advances characterizing the latest OLCI data products, are: *i.* the application of SVC to both OLCI-A and OLCI-B data in view of meeting the stringent accuracy requirements for the retrieval of $\rho_w^{OLCI}(\lambda)$ and ensure the necessary consistency to data products across missions; *ii.* an improved BPC; and finally, *iii.* the use of a spectrally-resolved whitecap correction to minimize the perturbing effects of foam as a function of wind speed.

The SVC *g*-factors for OLCI-A and OLCI-B, which are provided in Table 2 for the sole visible and key near-infrared bands, were determined relying on the basic principles applied for the majority of ocean color missions (see Franz et al., 2007) by assigning a constant value (generally 1) to the *g*-factor at the 865 nm center-wavelength and then successively addressing the determination of *g*-factors at the remaining center-wavelengths. Specifically, OLCI-A and OLCI-B Level-1 data from the South Pacific Gyre were used for the computation of the *g*-factors at the near-infrared bands λ_n with observation conditions characterized by oceanic aerosols and $\rho_w^{OLCI}(\lambda_n) = 0$ (*i.e.*, allowing the so-called black-pixel assumption for clear waters). Additionally, *in situ* hyperspectral water reflectance measurements $\rho_w^{MOBY}(\lambda)$ from the Marine Optical Buoy (MOBY) off Lanai in the Northern Pacific Ocean were applied to determine *g*-factors for the visible spectral bands (*i.e.*, those exhibiting center-wavelengths between 400 and 700 nm) with observation conditions also characterized by oceanic aerosols and oligotrophic waters.

In view of accounting for differences affecting OLCI-A and OLCI-B relative responsivity in the near-infrared, a unitary *g*-factor at 865 nm was taken for OLCI-B while it was scaled down by 1.4% for OLCI-A consistent with results from the analysis of data from the *Tandem Phase* (Lamquin et al., 2020a).

Overall, in agreement with the mean OLCI-A and OLCI-B inter-calibration determined after flat fielding for the *Tandem Phase* by Lamquin et al. (2020a), OLCI-A exhibits positive radiometric biases compared to OLCI-B with differences varying from approximately 2.5% in the blue down to 1.2% in the near-infrared. At 865 nm, the average difference

over all detectors and cameras was found to be about 1.375%. This value was used to define the OLCI-A *g*-factor of 0.986, with a standard assumption of a unit gain for OLCI-B. It is recalled that OLCI-B data products from the previous processing (*i.e.*, Baseline 2) did not benefit of any SVC (*i.e.*, the *g*-factors were all assumed equal to 1). On the contrary, OLCI-A *g*-factors determined for the Baseline 2, were determined with an interim strategy combining various *in situ* measurements as well as satellite climatology from the GlobCOLOUR dataset (Maritorena et al., 2010).

BPC, which is a critical step preceding the atmospheric correction of data for optically turbid waters, quantifies the potential water signal in the near-infrared bands to allow the confident application of the basic atmospheric correction approach that assumes $\rho_w^{OLCI}(\lambda_n) = 0$ with $\lambda_n > 700$nm. The BPC scheme supporting the Operational Baseline 3 Collection OL_L2M.003.01 and successive products, uses an iterative algorithm relying on a coupled water-atmosphere model applied to the near-infrared spectral bands centred at 709, 753, 779, 865, 885 and 1020 nm (Mazeran et al., 2021). It is emphasized that the recent inclusion of the band at 1020 nm was shown to further improve BPC retrievals in highly turbid waters (Hieronymi et al., 2021). Also, in view of ensuring spatial consistency to ocean color data products, BPC is applied to each pixel regardless of the water type.

The whitecap correction combines whitecap spectral reflectance and spatial coverage (*i.e.*, the fraction of water surface covered by foam). The whitecap reflectance implemented for correcting foam perturbations for the Operational Baseline 3 Collection OL_L2M.003.01 data and successive data releases (EUMETSAT, 2021a), follows the general principles detailed in Mobley et al. (2016). Briefly, it combines the effective whitecap irradiance reflectance (Koepke, 1984) and spectral normalized reflectance factor (Frouin et al., 1996). The whitecap spatial coverage, which largely increases with wind speed *v*, is that proposed for unde-veloped seas with $6.33 \leq v \leq 12.0$ m s^{-1} (Stramska and Petelski, 2003). In fact, below 6.33 m s^{-1} the whitecap effects are negligible. On the contrary, beyond 12.0 m s^{-1} the sea surface is too perturbed for an accurate determination of the foam coverage and the pixels are flagged accordingly.

As already anticipated, the OLCI OCR quantity assessed in this study is the spectral normalized water-leaving radiances $L_{WN}^{OLCI}(\lambda)$ determined from the Level-2 $\rho_w^{OLCI}(\lambda)$ through the standard processing, as

$$L_{WN}^{OLCI}(\lambda) = \rho_w^{OLCI}(\lambda) \frac{E_0(\lambda)}{\pi} C_{f/Q}(\lambda) \tag{1}$$

where $E_0(\lambda)$ is the mean extraterrestrial solar irradiance (Thuillier et al., 2003) and $C_{f/Q}(\lambda)$ a correction term for the bidirectional effects (Morel et al., 2002).

OLCI-A and OLCI-B data have been considered for the construction of matchups (pairs of *in situ* and satellite data) when not affected by the following recommended flags (EUMETSAT, 2019, 2021a): *CLOUD, CLOUD_AMBIGUOUS, CLOUD_MARGIN, INVALID, COSMETIC, SATU-RATED, SUSPECT, HISOLZEN, HIGHGLINT, SNOW_ICE, AC_FAIL, WHITECAPS, ADJAC, RWNEG_O2, RWNEG_O3, RWNEG_O4, RWNEG_O5, RWNEG_O6, RWNEG_O7, RWNEG_O8*. A comprehensive analysis of the impact of these flags is out of the scope of this work. Nevertheless, it is of interest to document that the *HIGHGLINT* flag strictly related to the illumination and observation geometry, affected approximately 5–6% and 10–15% of the high- and mid-latitude potential matchups, respectively.

Table 2

OLCI-A and OLCI-B *g*-factors applied for the Operational Baseline 3 Collection OL_L2M.003.01 (*g*-factors for each spectral band are provided in EUMETSAT (2021a)). The spectral bands are identified by their center-wavelengths λ in units of nm.

λ	400.0	412.5	442.5	490.0	510.0	560.0	620.0	665.0	778.8	865.0
OLCI-A	0.97546	0.97406	0.97492	0.96890	0.97184	0.97571	0.98001	0.97834	0.98772	0.986
OLCI-B	0.99458	0.99010	0.99221	0.98620	0.98898	0.99114	0.99769	0.99684	1.00259	1.000

2.2. VIIRS-S data products

The capability to address climate change investigations with OCR data products, requires decadal time series and the possibility to concatenate products exhibiting high temporal stability and high accuracy from successive satellite missions. To provide a further indirect term of reference for the OLCI-A and OLCI-B data products, and additionally to evaluate accuracies characterizing data products from fully independent missions candidate to support the creation of CDRs, VIIRS-S data products have been also assessed using the same scheme applied to OLCI-A and OLCI-B data. Specifically, VIIRS-S and AERONET-OC matchup data are analyzed and presented at the center-wavelengths 410, 443, 486, 551, 671 nm. Band-shift corrections have been applied to AERONET-OC data to match the center-wavelengths of the satellite sensor (Zibordi et al., 2009a). It is mentioned that the choice of VIIRS-S with respect to other ocean color sensors, was simply suggested by the consolidated stage of the related data products.

Level-1A VIIRS-S data were processed with SeaDAS version 7.5 (Mobley et al., 2016 and references therein) generating Level-2 data with 0.75-km resolution consistent with NASA's Ocean Biology Processing Group (OBPG) Reprocessing R2018 and the latest calibration table. It is recalled that VIIRS-S SVC was performed in agreement with Franz et al. (2007): this is expected to ensure the highest consistency among OLCI-A, OLCI-B and VIIRS-S radiometric products, contrary to the application of SVC schemes relying on different methodologies or diverse *in situ* reference data.

In agreement with the scheme applied in this work, VIIRS-S standard Level-2 spectral remote sensing reflectance $R_{RS}^{VIIRS-S}(\lambda)$ products already corrected for the bidirectional effects consistently with Morel et al. (2002), have been converted to spectral normalized water-leaving radiances $L_{WN}^{VIIRS-S}(\lambda)$ according to

$$L_{WN}^{VIIRS-S}(\lambda) = R_{RS}^{VIIRS-S}(\lambda) \cdot E_0(\lambda) \tag{2}$$

where, as for OLCI-A and OLCI-B data reduction, $E_0(\lambda)$ is from Thuillier et al. (2003).

VIIRS-S data have been considered for matchups when not affected by the following flags (NASA, 2021): *ATMFAIL, LAND, HIGLINT, HILT, HISATZEN, STRAYLIGHT, CLDICE, HISOLZEN, LOWLW, CHLFAIL, NAVWARN, MAXAERITER, CHLWARN, ATMWARN, NAVFAIL*. In the case of VIIRS-S, the *HIGLINT* flag affected less than 1% and approximately 1–4% of the high- and mid-latitude potential matchups, respectively.

2.3. AERONET-OC in situ reference data

The *in situ* reference data applied to assess the accuracy of satellite OCR products are Level-2 or, when not available, Level-1.5 AERONET-OC data from the Version-3 database (Zibordi et al., 2021). It is briefly recalled that Level-1.5 data, usually applied for almost real time applications, do not benefit of the post-deployment calibrations of the field radiometer, and of additional quality controls such as the spectrum-by-spectrum check by an experienced scientist.

AERONET is a federated measurement network managed by the Goddard Space Flight Center (GSFC) of the U.S. National Aeronautics and Space Administration (NASA) specifically developed to support aerosol investigations through standardized instruments and methods (Holben et al., 1998, 2001). Equivalent to AERONET, AERONET-OC relies on NASA's infrastructure for field instrument calibration, data processing and archiving, and benefits of commitments by the Joint Research Centre (JRC) for the quality control of data products (Zibordi et al., 2021). These activities are complemented by field actions addressed to establishing and maintaining CE-318 and CE-318 T modified sun-photometers at specific measurement sites. These instruments have the capability of performing autonomous above-water radiometric measurements in addition to the common AERONET atmospheric ones.

AERONET-OC deployment requirements for the collection of measurements suitable for OCR validation activities imply (Zibordi et al., 2021): *i.* fixed offshore structures allowing for measuring the direct sun irradiance through accurate sun-tracking; *ii.* superstructures with height and shape minimizing contamination of the measuring system by sea-spray; and *iii.* deployment positions allowing unobstructed sea observations at the maximum possible distance from the superstructure at the time of satellite overpass; *iv.* distance from the mainland allowing to assume that the adjacency effects are negligible in the remote sensing data; and finally *v.* water depth ensuring negligible bottom perturbations.

Key features of AERONET-OC are: *i.* near-real time data collection and processing (*i.e.*, within a few hours); *ii.* use of a standardized instrument, calibration procedure and data processing; *iii.* open access to measurements and data products.

The primary data product of AERONET-OC is the spectral normalized water-leaving radiance $L_{WN}(\lambda)$ (hereafter referred to as $L_{WN}^{PRS}(\lambda)$) at center-wavelengths λ of relevance for satellite ocean color applications. An additional product is the spectral aerosol optical depth $\tau_a(\lambda)$ (hereafter $\tau_a^{PRS}(\lambda)$) complemented by phase function, particle size distribution and single scattering albedo of aerosols, all having potential importance to assess the performance of the atmospheric correction applied to satellite data. AERONET-OC data benefit of a number of quality assurance / control criteria and well respond to requirements for the validation of satellite data products: accessibility, representativity over a wide range of observation conditions, traceability to SI, and quantified uncertainties (even though the latter were not determined for all measurement sites). An additional qualifying element of AERONET-OC is the generation of time-series providing the potential for addressing investigations across inter- and intra-annual cycles.

Relative uncertainties affecting $L_{WN}^{PRS}(\lambda)$ largely vary from region to region because of the diverse water types and illumination conditions. An extended evaluation of these uncertainties indicated values close to 5% in the blue-green and reaching 8% in the red for mid-latitude moderately turbid waters (Zibordi et al., 2009b), but approaching 30% in the blue at sites exhibiting very low water-leaving radiance such as those from the highly absorbing waters of the Baltic Sea (Gergely and Zibordi, 2014).

The uncertainties affecting individual $L_{WN}^{PRS}(\lambda)$ applied in the following analysis, were quantified statistically as a function of the $L_{WN}^{PRS}(\lambda)$ value in agreement with Zibordi et al. (2022). Nevertheless, $L_{WN}^{PRS}(\lambda)$ uncertainties do not contribute to the determination of the statistical indices used for the assessment of satellite ocean color data products. They are only displayed in scatter plots to more quantitatively support the comparison of *in situ* and satellite radiometric data products.

The analysis proposed in this work relies on AERONET-OC data exclusively collected with CE-318 T marine instruments systematically deployed at JRC sites since 2018. These instruments have spectral bands matching the major OLCI ocean color ones in the visible spectral region (*i.e.*, those with nominal center-wavelengths of 400, 412.5, 442.5, 490, 510, 560, 620, 665 nm). Additional bands characterizing the CE-318 T instruments with spectral configuration conceived for marine investigations, are those centered at 779 and 865 nm expected to support the assessment of the aerosol data by-products from the atmospheric correction process.

The AERONET-OC sites included in this study are grouped accounting for regional water types. These sites are (see Fig. 1): *i.* Casablanca Platform (CPL: Lat. 40.717°, Lon. 1.358°) in the Western Mediterranean Sea; *ii.* Gloria (GLR; Lat. 44.600°, Lon. 29.360°), Section-7 Platform (ST7: Lat. 44.546°, Lon. 29.447°) and Galata Platform (GLT: Lat. 43.045°, Lon. 28.193°) in the Western Black Sea, and Acqua Alta Oceanographic Tower (AAOT: Lat. 45.314°, Lon. 12.508°) in the northern Adriatic Sea; and finally *iii.* Gustaf Dalen Lighthouse Tower (GDLT: Lat. 58.594°, Lon. 17.467°), Irbe Lighthouse (ILT: Lat. 57.751°, Lon. 21.7230°), and Helsinki Lighthouse Tower (HLT: Lat. 59.949°, Lon. 24.926°) in the Baltic Sea.
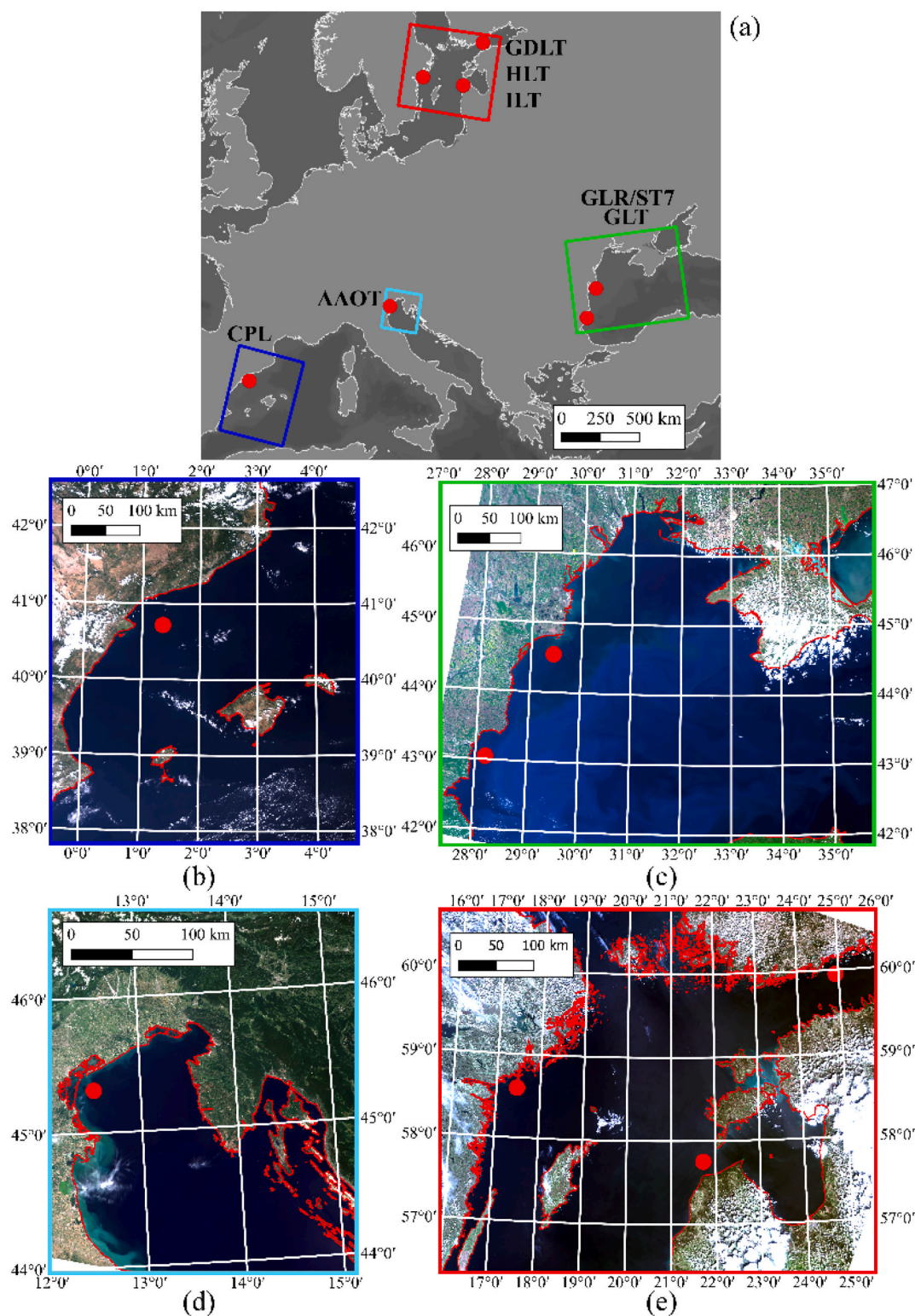
Fig. 1. Locations (a) of the AERONET-OC sites included in the assessment: (b) Casablanca Platform (CPL) in the Western Mediterranean Sea; (c) Gloria (GLR), Section-7 (ST7) and Galata (GLT) platforms in the Western Black Sea; (d) Acqua Alta Oceanographic Tower (AAOT) in the northern Adriatic Sea; and (e) Gustaf Dalen (GDLT), Irbe (ILT) and Helsinki (HLT) Lighthouses in the Baltic Sea.

The selected sites well represent waters characterized by diverse bio-optical features (see Berthon et al., 2008), and specifically: *i.* low Chl*a* concentration in the Western Mediterranean Sea, leading to frequent occurrence of oligotrophic/mesotrophic Case-1 conditions (*i.e.*, exhibiting optical features determined by Chl*a*) as obtained by retaining for successive analysis those $L_{WN}^{PRS}(\lambda)$ spectra exhibiting maxima at center-wavelengths $\lambda < 490$ nm; *ii.* various concentrations of sediments and chromophoric dissolved organic matter (CDOM) in the Black Sea and northern Adriatic Sea, all representative of generic optically complex waters; and finally *iii.* high concentrations of CDOM in the Baltic Sea.

The aerosol type is mostly continental with maritime influence at all the sites (Mélin et al., 2013). This property is generally intrinsic of all

AERONET-OC sites due to their coastal nature.

AERONET-OC data are corrected for differences in center-wavelengths with respect to those of the satellite sensor ones. This correction, which relies on regional bio-optical band-ratio algorithms to determine the total absorption and backscattering coefficients of water (Zibordi et al., 2009a), is minor for OLCI-A and OLCI-B matchups because the CE-318 T AERONET-OC center-wavelengths specifically match those of the two satellite sensors. Corrections may become significant at some center-wavelengths for VIIRS-S matchups.

It is noted that all the AERONET-OC data included in the following analysis are from Level-2, except those from ST7 and CPL for which Level-1.5 data were the only available due to delays in the annual rotation of the instrument during 2020 and early 2021.

Finally it is recalled that most of the AERONET-OC sites relevant to this study are located in coastal regions. Their distance from the mainland exceeds several nautical miles (*i.e.*, it varies from 8 nautical miles for the AAOT up to 25 nautical miles for CPL), which minimizes adjacency effects in satellite data.

2.4. Assessment criteria

Matchups of satellite (either OLCI-A, OLCI-B or VIIRS-S) and *in situ* data (*i.e.*, AERONET-OC) have been constructed using the mean of the 3×3 satellite pixels centred at the measurement sites. By targeting the need to maximize best comparability of satellite and *in situ* data, matchups have been retained for successive analysis when: *i.* the time difference Δt between *in situ* measurement and satellite overpass is less than ± 2 h (the AERONET-OC value closest in time to the satellite overpass has been considered); *ii.* none of the 3×3 pixels is affected by the standard processing flags; *iii.* the coefficient of variation (*i.e.*, the ratio of standard deviation to mean) of $L_{WN}^{OLCI-A}(\lambda)$, or $L_{WN}^{OLCI-B}(\lambda)$, or $L_{WN}^{VIIRS-S}(\lambda)$, is lower than 20% at 560 nm (or equivalent center-wavelength) for the nine pixels; *iv.* the viewing angle is lower than 60°; *v.* the sun zenith angle is lower than 70°; and *vi.* the aerosol optical depth τ_a determined at a near-infrared center-wavelength (*i.e.*, 865 nm for OLCI-A and OLCI-B, and 862 nm for VIIRS-S) is lower than 0.5.

The $L_{WN}(\lambda)$ analyses focused on the center-wavelengths λ comprised between 400 to 700 nm. Assessments of the normalized water-leaving radiance at longer center-wavelengths, regardless of the availability of the *in situ* reference data (*e.g.*, at 785, 865 and 1020 nm) were not attempted. This is justified by the relatively large uncertainties affecting AERONET-OC $L_{WN}^{PRS}(\lambda)$ in the near-infrared spectral bands across most water types and to a lesser extent, by the lack of corrections for bidirectional effects (Zibordi et al., 2021).

OCR by-products, *i.e.*, the optical depth τ_a at a single near-infrared center-wavelength and the Ångström exponent α expressing its spectral dependence, have been also investigated as they are relevant for an evaluation of the atmospheric correction performance and of the sensor calibration accuracy at the near-infrared bands. The satellite derived α (hereafter α^{OLCI-A}, α^{OLCI-B} and $\alpha^{VIIRS-S}$) are determined from the sole aerosol optical depths at the bands centered at 779 and 865 nm in the case of OLCI, and 746 and 862 nm in the case of VIIRS-S. On the contrary, to minimize the impact of measurement noise, AERONET-OC derived α (hereafter α_r^{PRS}) have been determined from aerosol optical depths at the 665, 779 and 870 nm center-wavelengths.

Uncertainty requirements for satellite radiometric products (*e.g.*, EUMETSAT, 2019) are commonly defined by a spectrally and water type independent "5% uncertainty" (which should be more comprehensively defined as a " 5% uncertainty target for satellite ocean-color radiometric products from oligotrophic and mesotrophic oceanic waters in the blue-green spectral regions" (World Meteorological Organization (WMO), 2011; Zibordi and Voss, 2014). Definitively the generic "5% uncertainty" requirement, is currently unrealistic for OCR data products from optically complex waters and consequently does not allow to set specific uncertainty targets for this assessment study, except for the oligotrophic/mesotrophic water case.

Satellite data products are evaluated through qualitative and quantitative comparisons. The qualitative assessment is performed through a visual examination of *in situ* and satellite $L_{WN}(\lambda)$ spectra. The main purpose of such an evaluation is to highlight artifacts that may characterize either satellite or *in situ* data.

The quantitative assessment performed for $L_{WN}(\lambda)$, τ_a in the near-infrared, and α, is accomplished through the determination of statistical indices for the N matchups of satellite (*SAT*) and *in situ* (*PRS*) data $[(\mathfrak{I}_1^{SAT}, \mathfrak{I}_2^{SAT}, ..., \mathfrak{I}_N^{SAT}), (\mathfrak{I}_1^{PRS}, \mathfrak{I}_2^{PRS}, ..., \mathfrak{I}_N^{PRS})]$ where $\mathfrak{I}$ is the compared quantity (*e.g.*, $L_{WN}(\lambda)$), and the subscripts 1, 2 …, N indicate the matchup index. The statistical indices are: the median of differences Δ_m and the median of absolute (unsigned) differences $|\Delta|_m$; the median of relative differences ψ_m and the median of absolute (unsigned) relative differences $|\psi|_m$, both determined with respect to the *in situ* reference data; the root mean square of differences *rmsd*; and the determination coefficient r^2 from data regression. The indices $|\Delta|_m$ and $|\psi|_m$ provide hints on the dispersion of data, conversely Δ_m and ψ_m provide information on biases. The quantities $|\psi|_m$ and ψ_m are expressed in percent. On the contrary, $|\Delta|_m$, Δ_m and *rmsd* are in physical units (*e.g.,* mW cm^{-2} μm^{-1} sr^{-1} for L_{WN}). While indices in percent provide immediate feedback on the comparisons, the indices in physical units complement the former information with statistics strictly related to the values and range of the quantities assessed.

The use of the *median* with respect to the *mean* allows to better determine the *centrality* of the comparison results. This solution is suggested by the appreciation that the values of the compared quantities $\mathfrak{I}$, may not exhibit ideal normal distribution. Finally, to minimize the impact of potential outliers, $|\psi|_m$ and ψ_m are computed excluding any individual value exceeding two standard deviations from the mean (this filtering scheme is mostly effective with a relatively low number of matchups).

Considering the need to best support the comparison of statistical results from this study with those from independent ones likely resulting from matchup data sets constructed with different *in situ* reference data or from other geographic regions, the median *m* and the median absolute deviation μ of the *in situ* reference data are provided for each compared quantity and comparison case. The quantity μ is a measure of the statistical dispersion of data points around their *median* with $\mu = median[|(\mathfrak{I}_1, \mathfrak{I}_2, ..., \mathfrak{I}_N) - median(\mathfrak{I}_1, \mathfrak{I}_2, ..., \mathfrak{I}_N)|]$ where $\mathfrak{I}_i = \mathfrak{I}_1, \mathfrak{I}_2, ..., \mathfrak{I}_N$ indicates the quantity included in the comparison, and the subscript *i* is the matchup index. When compared to the standard deviation, μ is much less influenced by outliers.

All the values for the above statistical indices are included in figures or alternatively in tables in view of providing a comprehensive overview on the quality of the OCR data products analyzed in this study. These values also set a term of reference for alternative investigations relying on different measurements and sites. However, for the benefit of conciseness, only a few parameters and values will be presented and discussed in the text. Finally, unless assuming negligible the uncertainties affecting the *in situ* data and the spatio-temporal effects (*i.e.*, the perturbations due to time difference and diverse spatial resolution of *in situ* and satellite data, still minimized by the application of a threshold to Δt), none of the above statistical quantities is a direct quantification of the uncertainties affecting satellite data, but only a conservative estimate of their values.

3. Results

Results from the matchup analysis of OCR data products are separately presented for the different regional waters, for $L_{WN}^{OLCI-A}(\lambda)$, $L_{WN}^{OLCI-B}(\lambda)$ and $L_{WN}^{VIIRS-S}(\lambda)$, and additionally for the by-products from the atmospheric correction, $\tau_a^{OLCI-A}(865)$, $\tau_a^{OLCI-B}(865)$, $\tau_a^{VIIRS-S}(862)$, α^{OLCI-A}, α^{OLCI-B} and $\alpha^{VIIRS-S}$.

3.1. OLCI-A

The matchup spectra of $L_{WN}^{OLCI-A}(\lambda)$ from OLCI-A and $L_{WN}^{PRS}(\lambda)$ from AERONET-OC, are displayed in Fig. 2 for the different regional waters types. Conversely, scatter plots are separately presented for each regional water type and center-wavelength in Figs. 3–5 together with the values of the relevant statistical indices.

The matchups for CPL oligotrophic/mesotrophic waters, likely representing Case-1 conditions by having been restricted to the exclusive $L_{WN}^{PRS}(\lambda)$ spectra exhibiting maxima at the blue center-wavelengths, are shown in Figs. 2 and 3. Results indicate an overall good agreement with the largest differences between satellite and *in situ* measurements

showing values of ψ_m varying between -4% and $+6\%$ in the 400–560 nm spectral interval, and a maximum underestimate of -31% at 665 nm. However, *i.* neglecting the spatio-temporal effects, *ii.* considering an uncertainty of approximately 5% for the *in situ* data in the blue-green spectral region for clear and moderately turbid waters, and *iii.* assuming uncertainties add in quadrature, the values of $|\psi_m|$ varying between 7% and 13% at the 400–560 nm center-wavelengths and increasing up to 48% at 665 nm, indicate that $L_{WN}^{OLCI-A}(\lambda)$ data do not meet the generic 5% uncertainty requirement at a number of bands in the visible spectral region.

Results for generic optically complex waters at GLR, ST7, GLT and AAOT displayed in Figs. 2 and 4, show systematic underestimates with
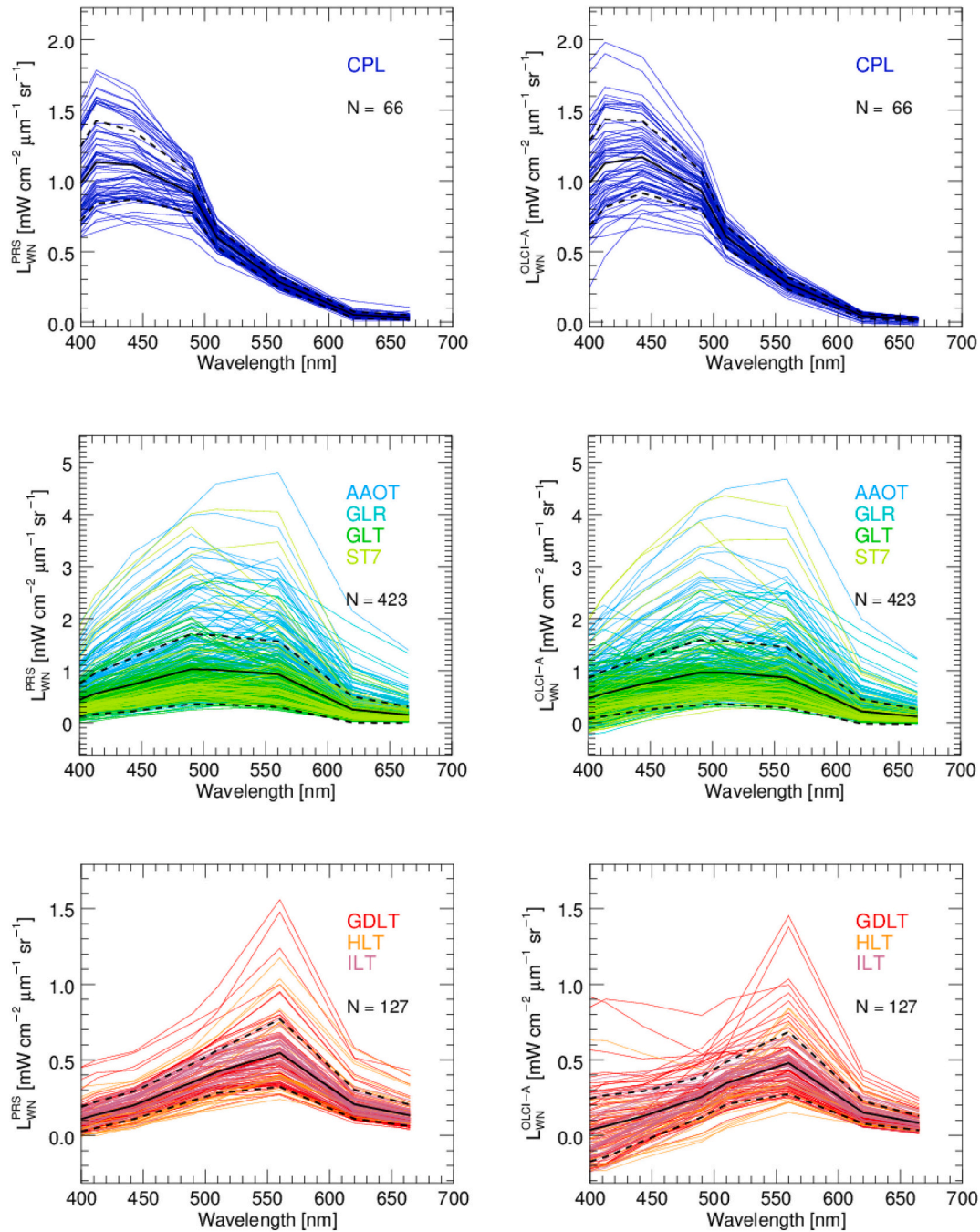

Fig. 2. AERONET-OC $L_{WN}^{PRS}(\lambda)$ and OLCI-A $L_{WN}^{OLCI-A}(\lambda)$ spectra, for different geographic water types (*i.e.*, oligotrophic-mesotrophic in the first row of panels; optically complex in the second row of panels; and optically complex, but dominated by high concentrations of CDOM, in the last row of panels). The continuous black lines indicate median values while the dashed black lines indicate ±1 standard deviation.
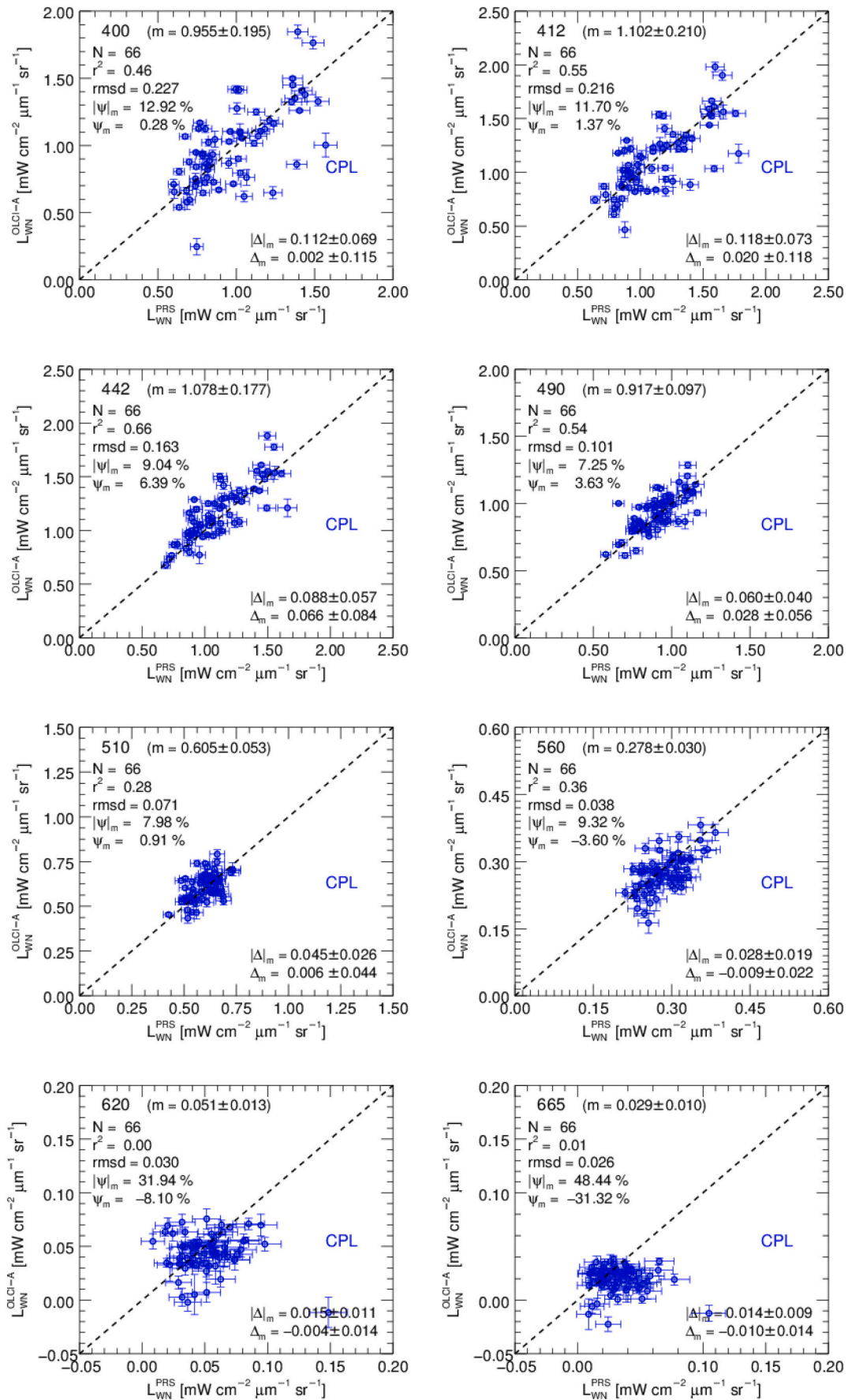
(caption on next page)

Fig. 3. Scatter plots of OLCI-A $L_{WN}^{OLCI-A}(\lambda)$ versus AERONET-OC $L_{WN}^{PRS}(\lambda)$ data for oligotrophic-mesotrophic waters at the CPL site, at the 400, 412, 442, 490, 510, 560, 620 and 665 nm center-wavelengths (with median and standard deviation of OLCI-A viewing and sun zenith angles $\theta^{OLCI-A} = 24.4° \pm 16.2°$ and $\theta_0 = 47.7° \pm 13.6°$, respectively). The error bars associated with the *in situ* data indicate measurement uncertainties while those related to satellite data indicate the variation coefficients determined from the 3×3 pixels contributing to matchups. N indicates the number of matchups, r^2 the determination coefficient, *rmsd* the root-mean square of differences, $|\psi|_m$ the median of unsigned percent differences, ψ_m the median of percent differences, $|\Delta|_m$ the median of unsigned differences and Δ_m the median of differences. The $\pm$ values associated with $|\Delta|_m$ and Δ_m are the median absolute deviations μ. The values in brackets aside the center-wavelength at the top of each panel, indicate the median $m \pm$ the related median absolute deviation μ of $L_{WN}^{PRS}(\lambda)$ at the specific center-wavelength λ.

ψ_m varying from -16% to -6%, except at 665 nm showing a value of -26%: this underestimate is less marked at the 442 nm center-wavelength exhibiting an overestimate at CPL. Still, the agreement between $L_{WN}^{OLCI-A}(\lambda)$ with $L_{WN}^{PRS}(\lambda)$ appears remarkable for the spectra exhibiting high values encompassing cases likely due to high coccolithophores and sediment concentrations occasionally characterizing the Western Black Sea (Cazzaniga et al., 2021).

Results for highly CDOM dominated waters at GDLT, ILT and HLT displayed in Figs. 2 and 5, show systematic and pronounced underestimates at all center-wavelengths as documented by the negative values of ψ_m exceeding several 10 %. This underestimate and the large dispersion of data, which is much more pronounced than that shown by the matchups representing generic optically complex waters, is actually enhanced by the small $L_{WN}^{OLCI-A}(\lambda)$ and $L_{WN}^{PRS}(\lambda)$ approaching nil values at the blue center-wavelengths. The $L_{WN}^{OLCI-A}(\lambda)$ spectra exhibiting the highest values are explained by the occurrence of summer cyanobacteria blooms in the Baltic Sea. The trends characterizing the values of Δ_m and $|\Delta|_m$, which are in absolute units and indicate increasing negative spectral biases rising with the optical complexity of water, further show a clear dependence of OLCI-A radiometric data products on water type. Such a dependence is not otherwise explained by diverse illumination and observation geometries as shown by the close values of the median of the sun zenith and also of the sensor viewing angles for the matchups representing the different water types.

Results from the analysis of $\tau_a^{OLCI-A}(865)$ and α^{OLCI-A} matchups are displayed in Fig. 6. Values of ψ_m varying from approximately 49% to 79% across the various regional waters, indicate systematically overestimated $\tau_a^{OLCI-A}(865)$. This overestimate, however, is more marked for matchups related to optically complex waters corresponding to sites probably more affected by continental aerosols. When analyzing results from the comparison of α^{OLCI-A} with α_r^{PRS}, the underestimate of α^{OLCI-A} is evident for all sites with maxima constrained below approximately 1.6 (while the *in situ* α_r^{PRS} exhibits values up to 3.0). This underestimate is underlined by the large occurrence of cases with $\alpha_r^{PRS} > 1.6$ leading to values of ψ_m in the range of -28% to -37%.

3.2. OLCI-B

Consistent with the format chosen for OLCI-A, matchup spectra of $L_{WN}^{OLCI-B}(\lambda)$ from OLCI-B and $L_{WN}^{PRS}(\lambda)$ from AERONET-OC are all displayed in Fig. 7 for the different regional waters. Conversely, results from inter-comparisons are separately proposed for each water type in Tables 3-5.

Results for CPL oligotrophic/mesotrophic waters summarized in Fig. 7 and Table 3, show statistical indices very consistent with those obtained for OLCI-A, with values of ψ_m within -6% and $+5\%$ in the 400–560 nm spectral interval, increasing up to -39% at 665 nm. Comparable to $L_{WN}^{OLCI-A}(\lambda)$, $L_{WN}^{OLCI-B}(\lambda)$ exhibits values of $|\psi_m|$ varying between 5% and 14% at the blue-green center-wavelengths, which also may suggest difficulty in meeting the 5% uncertainty requirement at some spectral bands.

Results for generic optically complex waters at GLR, ST7, GLT and AAOT shown in Fig. 7 and Table 4, are also fully consistent with those obtained for OLCI-A: *i.e.*, matchups indicate a systematic underestimate for OLCI-B $L_{WN}^{OLCI-B}(\lambda)$, less marked at 442 nm (*i.e.*, at the center-wavelength showing some appreciable overestimate at CPL). Also in this case, underestimates are slightly less pronounced than those determined for OLCI-A, with ψ_m ranging from -3% to -10% in the

400–560 nm spectral interval, approaching -14% at 620 nm and -26% at 665 nm.

Results for CDOM dominated waters at GDLT, ILT and HLT shown in Fig. 7 and Table 5, exhibit systematic and pronounced underestimates at all center-wavelengths. These underestimates, however, appear slightly more pronounced for OLCI-B than for OLCI-A at the 400 and 412 nm center-wavelengths. Finally, also consistent with results from OLCI-A, the dispersion quantified by $|\psi|_m$ and $|\Delta|_m$ is quite pronounced in the spectral interval between 400 and 490 nm for CDOM dominated waters.

Results from the assessment of $\tau_a^{OLCI-B}(865)$ and α^{OLCI-B} provided in Fig. 8 for all regional waters, also show statistics fully consistent with those obtained for OLCI-A with values of ψ_m varying from $+56\%$ to $+78\%$ for the aerosol optical depth and from -32% to -41% for the Ångström exponent. Equivalent to α^{OLCI-A}, also α^{OLCI-B} shows maxima constrained below approximately 1.6.

3.3. VIIRS-S data

Results from the comparison of $L_{WN}^{VIIRS-S}(\lambda)$ from VIIRS-S with $L_{WN}^{PRS}(\lambda)$ from AERONET-OC at CPL illustrated in Figs. 9 and 10, indicate spectral inconsistencies in the blue spectral region with systematic underestimates at 410 nm and minor overestimates at 443 nm revealed by ψ_m of -19% and $+4\%$, respectively. A large underestimate of $L_{WN}^{VIIRS}(\lambda)$ is also documented at 671 nm by $\psi_m = -56\%$. Nevertheless, very consistent results across the various regional water types, are displayed at 486 nm with ψ_m varying in the range of -2% to 0%, and at 551 nm with values of ψ_m in the range of -7% to -5%. This indicates a higher consistency of $L_{WN}^{VIIRS-S}(\lambda)$ accuracy across water-types with respect to $L_{WN}^{OLCI-A}(\lambda)$ and $L_{WN}^{OLCI-B}(\lambda)$, at least at two key center-wavelengths (*i.e.*, 486 and 551 nm as resulting from the comparison of Figs. 10, 11 and 12). Consistent with OLCI-A and OLCI-B OCR data products, also $L_{WN}^{VIIRS-S}(\lambda)$ from VIIRS-S shows higher dispersion of values at the blue center-wavelengths with respect to $L_{WN}^{PRS}(\lambda)$, increasing with the optical complexity of water.

The results from the analysis of the aerosol optical depth at 862 nm $\tau_a(862)$ provided in Fig. 13, show systematic overestimates. However, the values of $\tau_a^{VIIRS-S}(862)$ do not generally exceed 0.2. Additionally, the values of ψ_m, which vary from $+8\%$ for the oligotrophic/mesotrophic water site to $+33\%$ for the CDOM dominated water sites, indicate a lower overestimate with respect to the OLCI-A and OLCI-B by-product.

Results from the assessment of $\alpha^{VIIRS-S}$ also shown in Fig. 13, exhibit underestimated values and poor correlation between *in situ* and satellite derived values. Equivalent to OLCI-A and OLCI-B, results appear the worst for the sites representing optically complex waters. However, while α^{OLCI-A} and α^{OLCI-B} show values not exceeding 1.6, $\alpha^{VIIRS-S}$ exhibits values approaching 2.0 definitively allowed by a diverse set of candidate aerosol models (Ahmad et al., 2010). Lastly, ψ_m for $\alpha^{VIIRS-S}$ varies between -11% and -35%, generally exhibiting values as pronounced as those determined for OLCI-A and OLCI-B data.

A final note is necessary on the impact of the spatial resolution of VIIRS-S data products (0.75 km) higher than that of OLCI-A and OLCI-B Reduced-Resolution products (1.2 km). In fact, especially in costal optically complex waters, different spatial resolutions may impact results from the statistical assessments of data products. Because of this, an additional analysis restricted to the AAOT optically complex waters, has been made to evaluate the independence of results from the selection of 3×3 or alternatively 5×5 VIIRS pixels. Results (not shown) do not indicate any appreciable difference in the outcomes, except for a
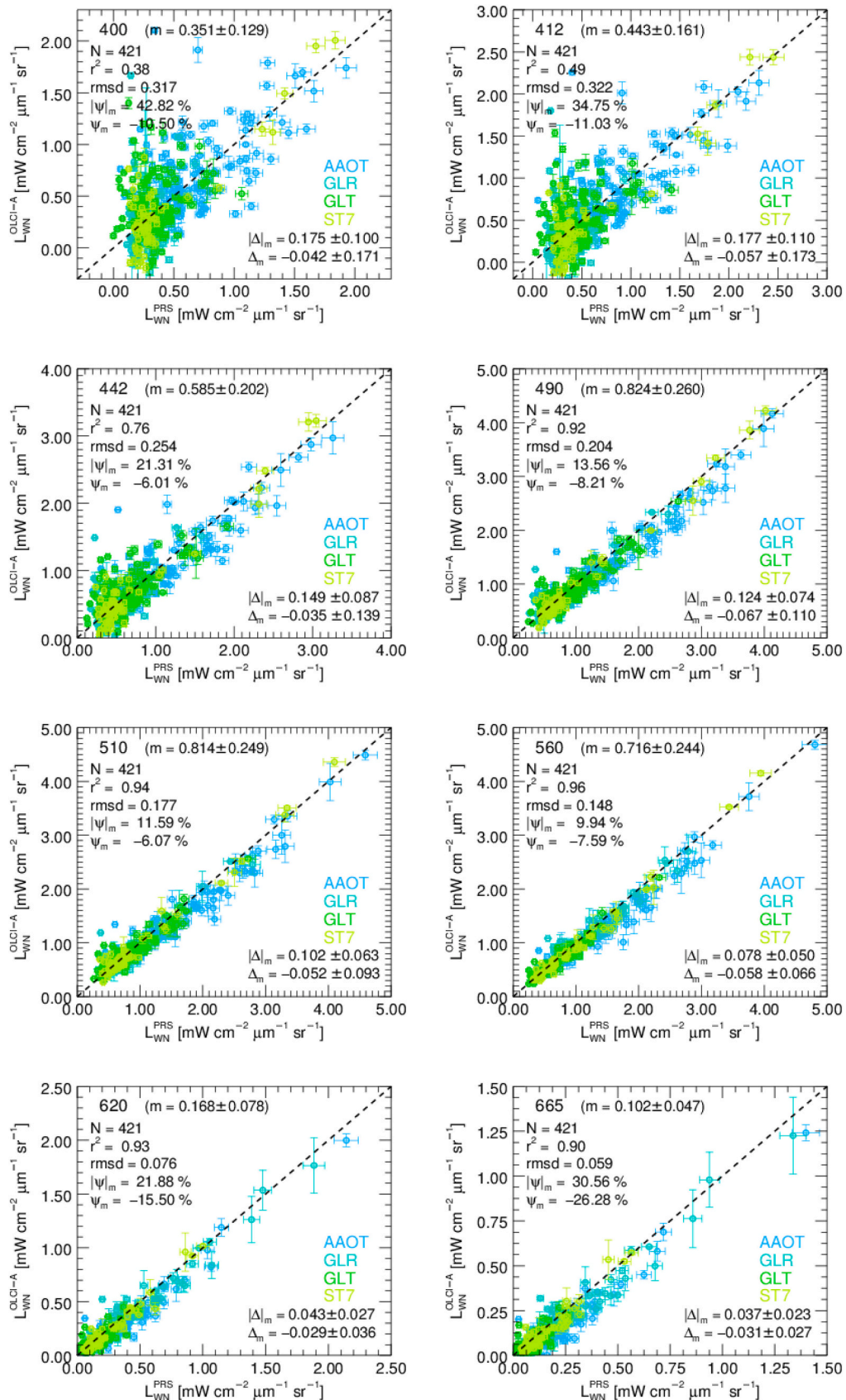
Fig. 4. Scatter plots of OLCI-A $L_{WN}^{OLCI-A}(\lambda)$ versus AERONET-OC $L_{WN}^{PRS}(\lambda)$ as in Fig. 3, but for optically complex waters at the AAOT, GLR, GLT and ST7 sites (with median and standard deviation of OLCI-A viewing and sun zenith angles $\theta^{OLCI-A} = 26.8° \pm 16.3°$ and $\theta_0 = 42.4° \pm 11.7°$, respectively).
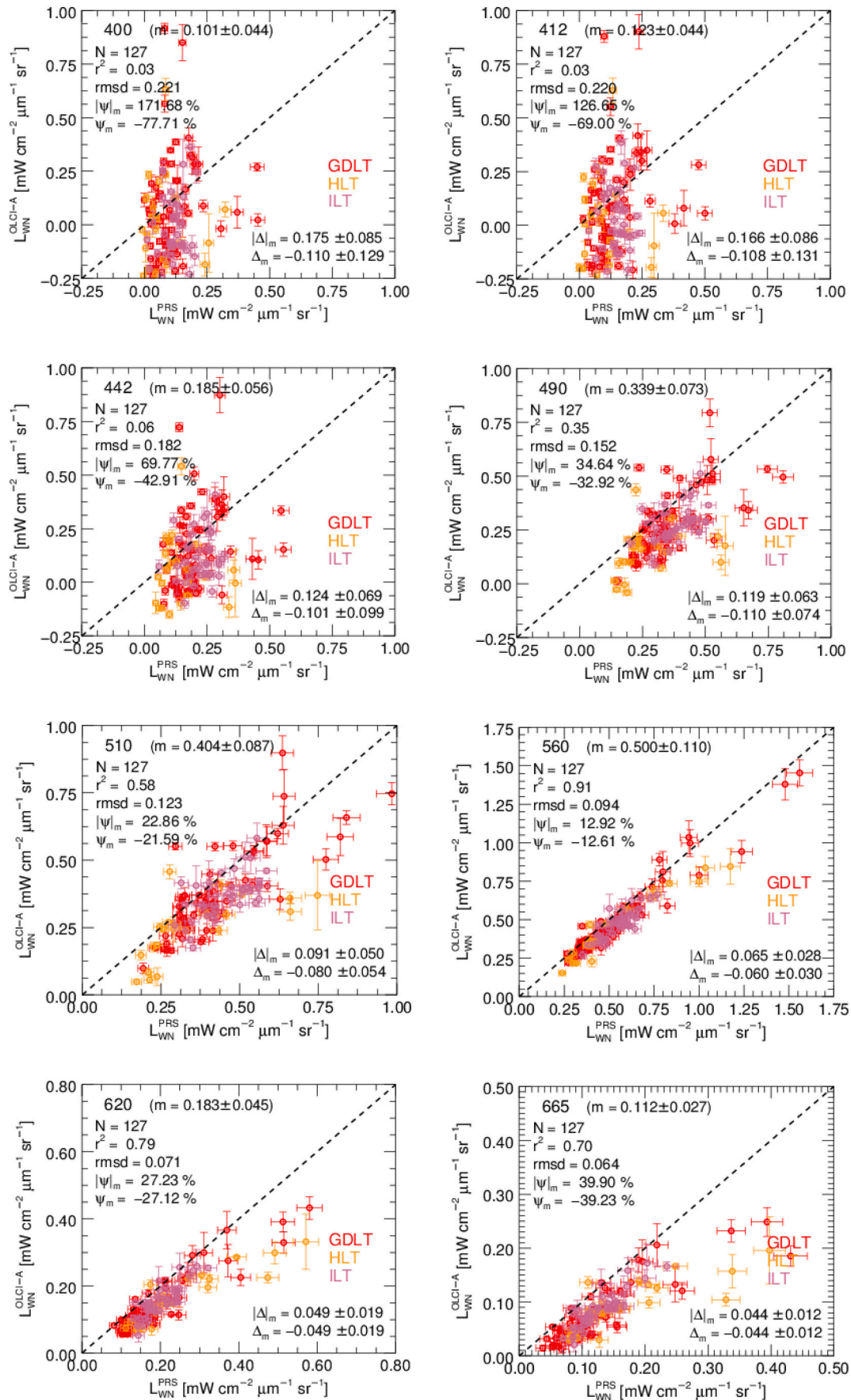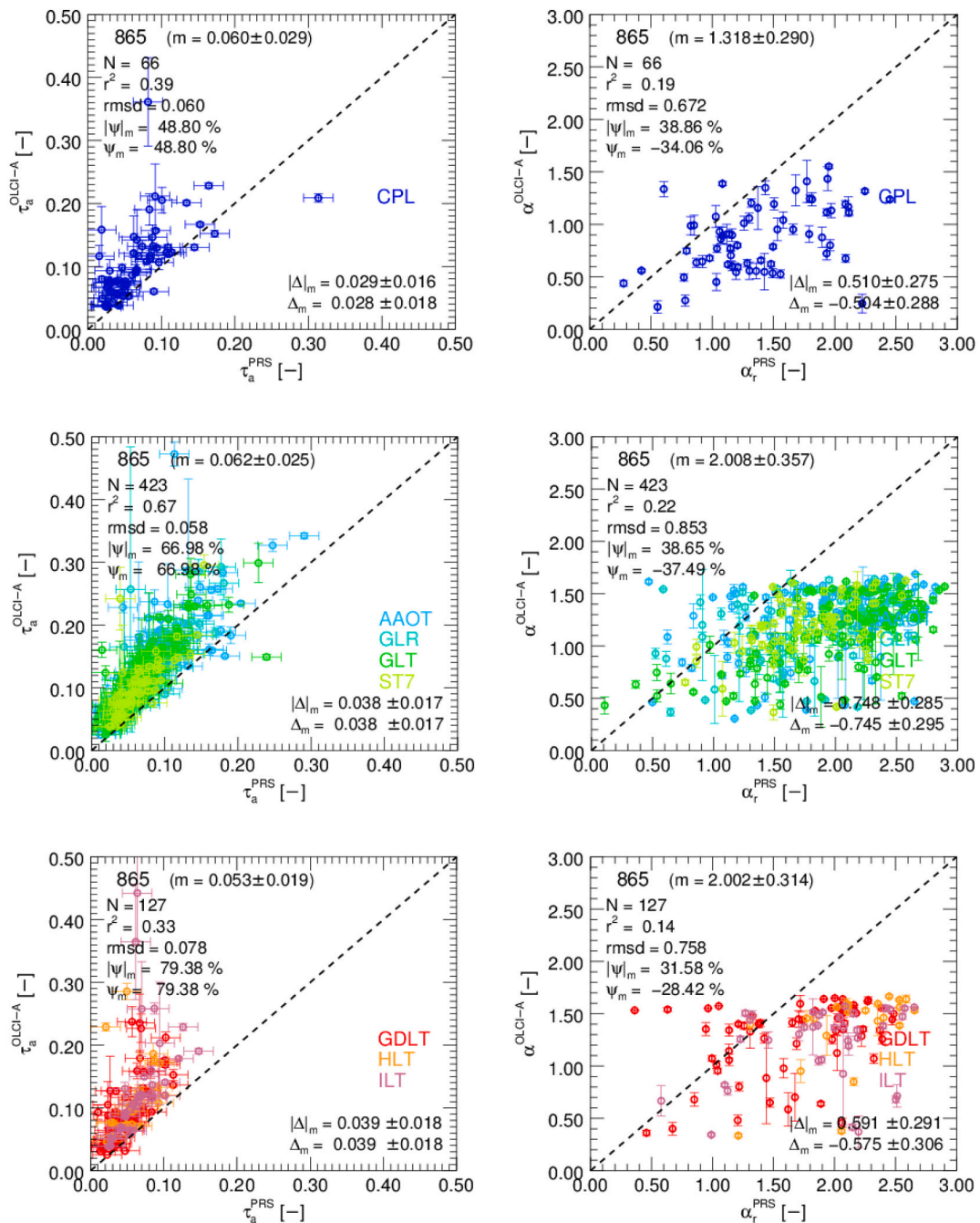
Fig. 5. Scatter plots of OLCI-A $L_{WN}^{OLCI-A}(\lambda)$ versus AERONET-OC $L_{WN}^{PRS}(\lambda)$ as in Fig. 3, but for CDOM dominated waters at the GDLT, HLT and ILT sites (with median and standard deviation of OLCI-A viewing and sun zenith angles $\theta^{OLCI-A} = 18.5° \pm 15.8°$ and $\theta_0 = 43.5° \pm 4.8°$, respectively).

Fig. 6. Scatter plots of OLCI-A $\tau_a^{OLCI-A}(865)$ versus AERONET-OC $\tau_a^{PRS}(865)$ data (panels in the first column) and of α^{OLCI-A} versus α_r^{PRS} (panels in the second column). The panels in the various rows refer to different water types (*i.e.*, oligotrophic-mesotrophic in the first row of panels; optically complex in the second row of panels; and optically complex, but dominated by high concentrations of CDOM in the last row of panels). The error bars associated with the *in situ* data indicate measurement uncertainties while those related to satellite data indicate the variation coefficients determined from the 3×3 pixels contributing to matchups. N indicates the number of matchups, r^2 the determination coefficient, *rmsd* the root-mean square of differences, $|\psi|_m$ the median of unsigned percent differences, ψ_m the median of percent differences, $|\Delta|_m$ the median of unsigned differences and Δ_m the median of differences. The $\pm$ values associated with $|\Delta|_m$ and Δ_m are the median absolute deviations μ. The values in brackets aside the center-wavelength at the top of each panel, indicate the median $m \pm$ the related median absolute deviation μ of $\tau_a^{PRS}(865)$ and α_r^{PRS}.

reduction of the number of matchups with the number of pixels chosen. This is explained by the matchup-construction scheme: all pixels of the 3×3 or 5×5 must satisfy specific criteria (*i.e.*, they must not be affected by distinct flags). Consequently, an increased number of pixels rises the probability that at least one of them does not satisfy the matchup construction criteria, which implies a potentially lower number of matchups.

4. Discussion

The analysis of OLCI-A and OLCI-B data products from the Operational Baseline 2 processing (Zibordi et al., 2018; Zibordi et al., 2019), showed spectral inconsistencies for OLCI-A $L_{WN}^{OLCI-A}(\lambda)$ and major systematic overestimates for OLCI-B $L_{WN}^{OLCI-B}(\lambda)$. Definitively, those main issues are solved in the current Operational Baseline 3 processing as a result of the comprehensive and cross-mission consistent SVC
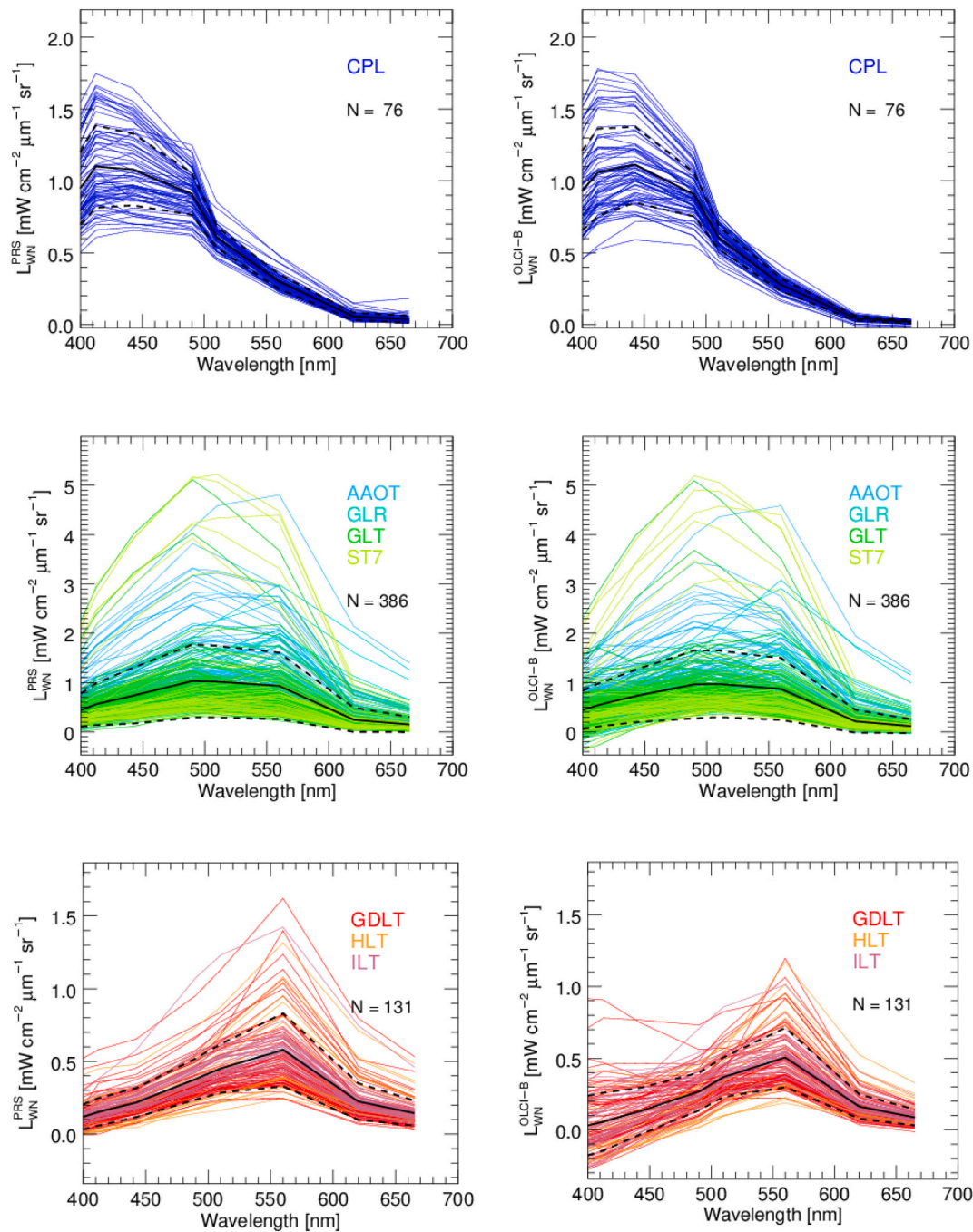
Fig. 7. AERONET-OC $L_{WN}^{PRS}(\lambda)$ and OLCI-B $L_{WN}^{OLCI-B}(\lambda)$ spectra, respectively, for different geographic water types (*i.e.*, oligotrophic-mesotrophic in the first row of panels; optically complex in the second row of panels; and optically complex, but dominated by high concentrations of CDOM in the last row of panels). The continuous black lines indicate median values while the dashed black lines indicate ± 1 standard deviation.

applied (EUMETSAT, 2021a). Still, a minor spectral inconsistency emerges from the current analysis at the 442 nm center-wavelength: evidence is provided by the values of ψ_m characterizing both $L_{WN}^{OLCI-A}(\lambda)$ and $L_{WN}^{OLCI-B}(\lambda)$ at 442 nm with respect to those determined for the nearby bands for both oligotrophic/mesotrophic and optically complex waters. This inconsistency could be explained by inaccuracies *i.* of the spectral parameters of the models embedded in the atmospheric correction code, *ii.* of instrument characterizations, *iii.* or even of the *in situ* data applied for SVC or products assessment. Nevertheless, none of the above hypotheses is supported by evidence.

An additional element emerging from the matchup analysis, common to both OLCI-A and OLCI-B, is an observed decrease of accuracy of $L_{WN}^{OLCI-A}(\lambda)$ and $L_{WN}^{OLCI-B}(\lambda)$ with an increase of the optical complexity of water, naturally ascribed to a decreased performance of the atmospheric correction. The increase in optical complexity, nevertheless, corresponds to an increase of the latitude of the various geographic regions included in the study. Still, a major dependence of $L_{WN}^{OLCI-A}(\lambda)$ and $L_{WN}^{OLCI-B}(\lambda)$ accuracy on the illumination geometry varying with latitude, should be basically excluded by the comparable median values of the sun zenith angles characterizing the ensemble of matchups representing the various water types (see the sun zenith values in the caption of Figs. 3–5 for OLCI-A and especially those in Tables 3-5 for OLCI-B).

Recognizing that the aerosol optical depth and the Ångström

Table 3

Summary results from OLCI-B $L_{WN}^{OLCI-B}(\lambda)$ and AERONET-OC $L_{WN}^{PRS}(\lambda)$ matchups analysis for oligotrophic/mesotrophic waters at CPL, at the 400, 412, 442, 490, 510, 560, 620 and 665 nm center-wavelengths.

	L_{WN}^{OLCI-B} vs L_{WN}^{PRS} $N = 76$, CPL, $\tau_a^{PRS}(870) = 0.051 \pm 0.020$, $\theta^{OLCI-B} = 32.1° \pm 12.6°$, $\theta_0 = 42.1° \pm 11.7°$							
λ [nm]	**400**	**412**	**442**	**490**	**510**	**560**	**620**	**665**
$m \pm \mu$	0.886 ± 0.178	1.036 ± 0.190	1.030 ± 0.163	0.908 ± 0.107	0.609 ± 0.050	0.300 ± 0.027	0.054 ± 0.015	0.033 ± 0.011
$\lvert\psi\rvert_m$ [%]	13.66	11.55	9.63	4.78	7.54	8.32	28.95	42.43
ψ_m [%]	−0.19	−2.16	+5.01	+1.58	+1.46	−6.19	−12.41	−38.50
$\lvert\Delta\rvert_m \pm \mu$	0.133 ± 0.083	0.129 ± 0.072	0.092 ± 0.053	0.045 ± 0.027	0.045 ± 0.027	0.025 ± 0.014	0.014 ± 0.008	0.015 ± 0.008
$\Delta_m \pm \mu$	-0.002 ± 0.135	-0.020 ± 0.121	$+0.049 \pm 0.091$	$+0.014 \pm 0.047$	$+0.009 \pm 0.044$	-0.018 ± 0.033	-0.008 ± 0.014	-0.014 ± 0.010
r^2 [−]	0.60	0.66	0.77	0.77	0.47	0.32	0.03	0.03
$rmsd$	0.179	0.185	0.131	0.074	0.061	0.051	0.031	0.030

N indicates the number of matchups, $\tau_a^{PRS}(870)$ the median ± the standard deviation of the *in situ* aerosol optical depth, θ^{OLCI-B} the median ± the standard deviation of the satellite sensor viewing angle and θ_0 the median ± the standard deviation of the sun zenith. The symbol m indicates the median of $L_{WN}^{PRS}(\lambda)$ at each center-wavelength λ, $\lvert\psi\rvert_m$ the median of unsigned percent differences, ψ_m the median of percent differences, $\lvert\Delta\rvert_m$ the median of unsigned differences, Δ_m the median of differences, r^2 the determination coefficient, $rmsd$ the root-mean square of differences. The ± values associated with m, $\lvert\Delta\rvert_m$ and Δ_m are the median absolute deviations μ. When not specified, the quantities are in units of mW cm^{-2} μm^{-1} sr^{-1}.

Table 4

As in Table 3, but for the optically complex waters at AAOT, GLR, GLT and ST7.

	L_{WN}^{OLCI-B} vs L_{WN}^{PRS} $N = 385$, AAOT & GLR & GLT & ST7, $\tau_a^{PRS}(870) = 0.065 \pm 0.049$, $\theta^{OLCI-B} = 27.5° \pm 15.9°$, $\theta_0 = 42.7° \pm 11.7°$							
λ [nm]	**400**	**412**	**442**	**490**	**510**	**560**	**620**	**665**
$m \pm \mu$	0.357 ± 0.130	0.454 ± 0.169	0.580 ± 0.193	0.824 ± 0.248	0.818 ± 0.224	0.725 ± 0.226	0.176 ± 0.076	0.103 ± 0.046
$\lvert\psi\rvert_m$ [%]	43.50	36.49	22.00	13.20	10.79	10.27	20.61	31.70
ψ_m [%]	−8.73	−9.81	−3.36	−7.24	−5.14	−7.06	−14.41	−25.96
$\lvert\Delta\rvert_m \pm \mu$	0.192 ± 0.113	0.185 ± 0.110	0.142 ± 0.084	0.113 ± 0.070	0.091 ± 0.060	0.076 ± 0.049	0.041 ± 0.027	0.036 ± 0.021
$\Delta_m \pm \mu$	-0.029 ± 0.177	-0.056 ± 0.169	-0.025 ± 0.139	-0.065 ± 0.097	-0.042 ± 0.084	-0.053 ± 0.067	-0.028 ± 0.032	-0.029 ± 0.025
r^2 [−]	0.42	0.54	0.80	0.94	0.95	0.96	0.93	0.90
$rmsd$	0.309	0.314	0.252	0.199	0.173	0.144	0.071	0.059

Table 5

As in Table 3, but for the CDOM dominated optically complex waters at GDLT, HLT, and ILT.

|	L_{WN}^{OLCI-B} vs L_{WN}^{PRS} $N = 131$, GDLT & HLT & ILT, $\tau_a^{PRS}(870) = 0.054 \pm 0.029$, $\theta^{OLCI-B} = 25.0° \pm 16.4°$, $\theta_0 = 43.5° \pm 5.3°$							
λ [nm]	**400**	**412**	**442**	**490**	**510**	**560**	**620**	**665**
$m \pm \mu$	0.108 ± 0.047	0.125 ± 0.042	0.201 ± 0.057	0.342 ± 0.079	0.407 ± 0.093	0.519 ± 0.130	0.187 ± 0.049	0.119 ± 0.034
$\lvert\psi\rvert_m$ [%]	181.41	149.71	73.93	35.48	22.39	13.41	28.00	40.50
ψ_m [%]	−112.90	−104.30	−47.92	−32.74	−20.14	−12.60	−27.57	−40.32
$\lvert\Delta\rvert_m \pm \mu$	0.190 ± 0.073	0.190 ± 0.073	0.145 ± 0.068	0.124 ± 0.064	0.094 ± 0.048	0.068 ± 0.029	0.053 ± 0.025	0.052 ± 0.020
$\Delta_m \pm \mu$	-0.132 ± 0.141	-0.137 ± 0.140	-0.107 ± 0.104	-0.121 ± 0.071	-0.082 ± 0.057	-0.066 ± 0.037	-0.053 ± 0.025	-0.052 ± 0.020
r^2 [−]	0.00	0.00	0.02	0.35	0.58	0.86	0.76	0.68
$rmsd$	0.239	0.240	0.196	0.166	0.137	0.122	0.090	0.077

exponent are by-products of the atmospheric correction, it is expected they can provide some insight on the correction process. Consistent with the former Operational Baseline 2, also the Operational Baseline 3 processing leads to a large overestimate of $\tau_a^{OLCI-A}(865)$ and $\tau_a^{OLCI-B}(865)$, and also a large underestimate of α^{OLCI-A} and α^{OLCI-B}. Compared to the products from the Operational Baseline 2 showing α^{OLCI-A} varying in a narrow interval around the 1.5 value (Zibordi et al., 2018), α^{OLCI-A} and α^{OLCI-B} from the Operational Baseline 3 show a much wider range of values, although confined below approximately 1.6. This finding suggests limitations in the determination of the aerosol models due to a restricted variety of aerosol types likely affecting the atmospheric correction process with effects increasing with wavelength decrease.

As an attempt to investigate the impact of the atmospheric correction on the underestimate of α^{OLCI-A} and α^{OLCI-B}, the matchup analysis has been repeated by restricting the selection criteria to *in situ* derived α_r^{PRS} lower than 2.0 to exclude those pairs exhibiting the largest deviation between *in situ* and satellite derived Ångström exponents. This solution, tested on OLCI-A matchups from optically complex waters (results not shown) leads to the exclusion of those L_{WN}^{OLCI-A} spectra exhibiting the

highest values at the blue center-wavelengths. This impacts the distribution of the spectra contributing to matchups with a minor decrease, with respect to the overall matchup data set, of the median radiance value at the blue center-wavelengths and, on the contrary, to an increase of the median radiance value at the green-red center-wavelengths. The ψ_m and Δ_m statistical indices from this re-analyses exhibit an increase of biases below 560 nm with $\alpha_r^{PRS} < 2.0$ (and conversely a decrease with $\alpha_r^{PRS} > 2.0$). Nevertheless, it appears challenging to draw any conclusion from these results. Consequently, although there is a potential link between the *in situ* $L_{WN}^{PRS}(\lambda)$ exhibiting the highest values at blue center-wavelengths and the satellite derived α^{OLCI-A} exhibiting the largest deviation from the *in situ* α_r^{PRS}, a firm statistical relation between the two was not identified.

A unique opportunity to assess the consistency of OLCI-A and OLCI-B data products, is offered by the so-called *Tandem Phase* that allowed the collection of data with Sentinel-3B and -3A flying 30 s apart on the same orbit (Clerc et al., 2020; Lamquin et al., 2020b). The *Tandem Phase* lasted from 7 June 2018 until 16 October 2018. It allowed the collection of OLCI-A and OLCI-B data at virtually the same time over the same locations, thus minimizing changes in data products due to diverse orbits
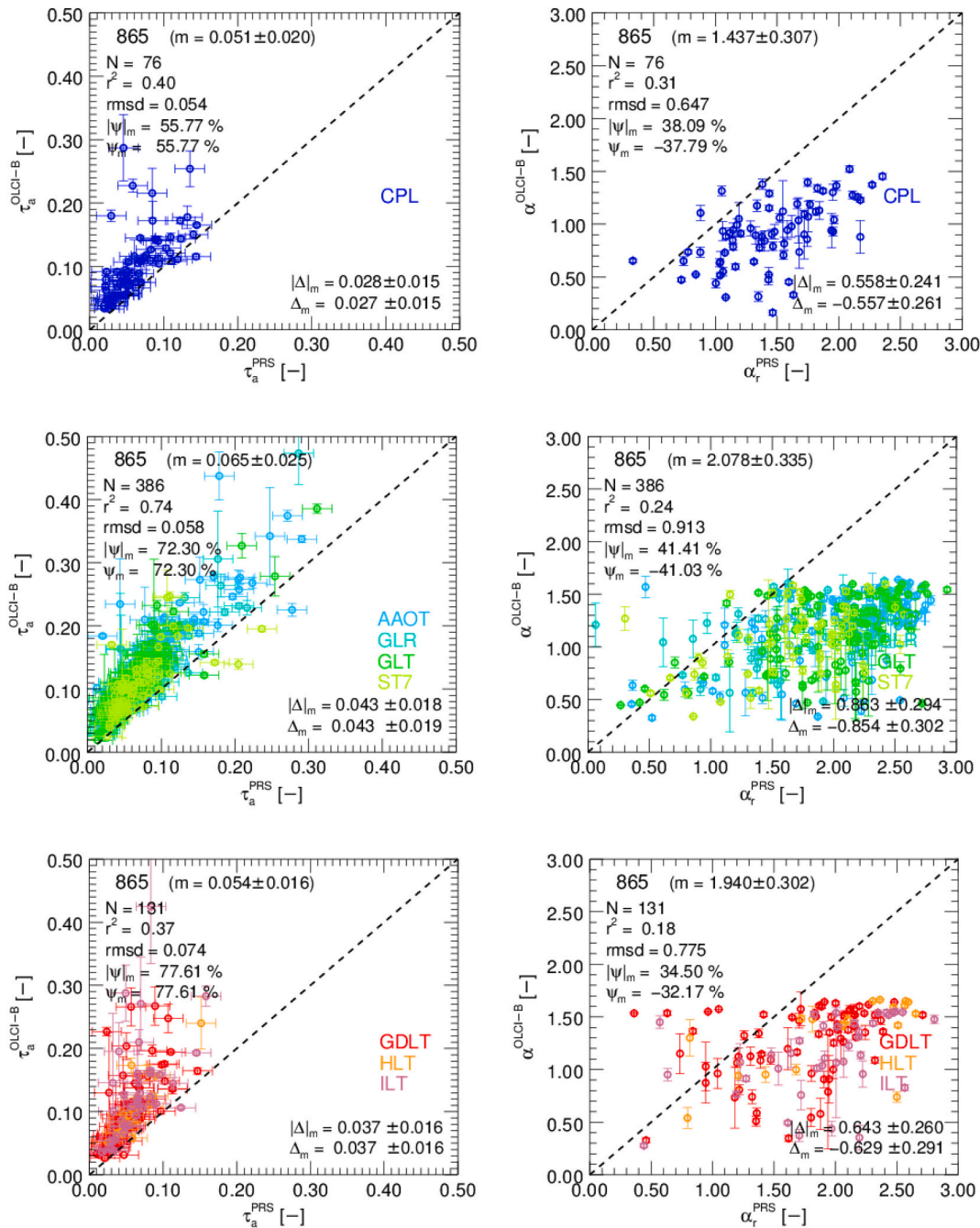
Fig. 8. Scatter plots of OLCI-B $\tau_a^{OLCI-B}(865)$ versus AERONET-OC $\tau_a^{PRS}(865)$ data (panels in the first column) and, of α^{OLCI-B} versus α_r^{PRS} (panels in the second column). The panels in the various rows refer to different water types (*i.e.*, oligotrophic-mesotrophic in the first row of panels; optically complex in the second row of panels; and optically complex, but dominated by high concentrations of CDOM in the last row of panels). The error bars associated with the *in situ* data indicate measurement uncertainties while those related to satellite data indicate the variation coefficients determined from the 3×3 pixels contributing to matchups. N indicates the number of matchups, r^2 the determination coefficient, *rmsd* the root-mean square of differences, $|\psi|_m$ the median of unsigned percent differences, ψ_m the median of percent differences, $|\Delta|_m$ the median of unsigned differences and Δ_m the median of differences. The $\pm$ values associated with $|\Delta|_m$ and Δ_m are the median absolute deviations μ. The values in brackets aside the center-wavelength at the top of each panel, indicate the median $m \pm$ the related median absolute deviation μ of $\tau_a^{PRS}(865)$ and α_r^{PRS}.

that would imply *i.* different viewing and illumination geometries, and *ii.* possible changes in marine and atmospheric features (including cloud perturbations).

The comparison of OLCI-B $L_{WN}^{OLCI-B}(\lambda)$ and OLCI-A $L_{WN}^{OLCI-A}(\lambda)$ has been performed for both the *Tandem Phase* and the successive period (in this latter case allowing a $\Delta t = \pm 1$ h), using 3×3 pixel extractions restricted to the *in situ* AERONET-OC optically complex water sites. Confining the analysis to AERONET-OC sites is an unnecessary

restriction when comparing OLCI-B $L_{WN}^{OLCI-B}(\lambda)$ and OLCI-A $L_{WN}^{OLCI-A}(\lambda)$, still it offers the possibility to investigate results from inter-comparisons related to locations benefitting of the assessments proposed in the former sections.

Results from the comparison of $L_{WN}^{OLCI-B}(\lambda)$ and $L_{WN}^{OLCI-A}(\lambda)$ are summarized in Fig. 14 for both the *Tandem Phase* and the successive period. Definitively, results from the *Tandem Phase* exhibit a remarkable agreement documented by spectrally averaged values of ψ_m
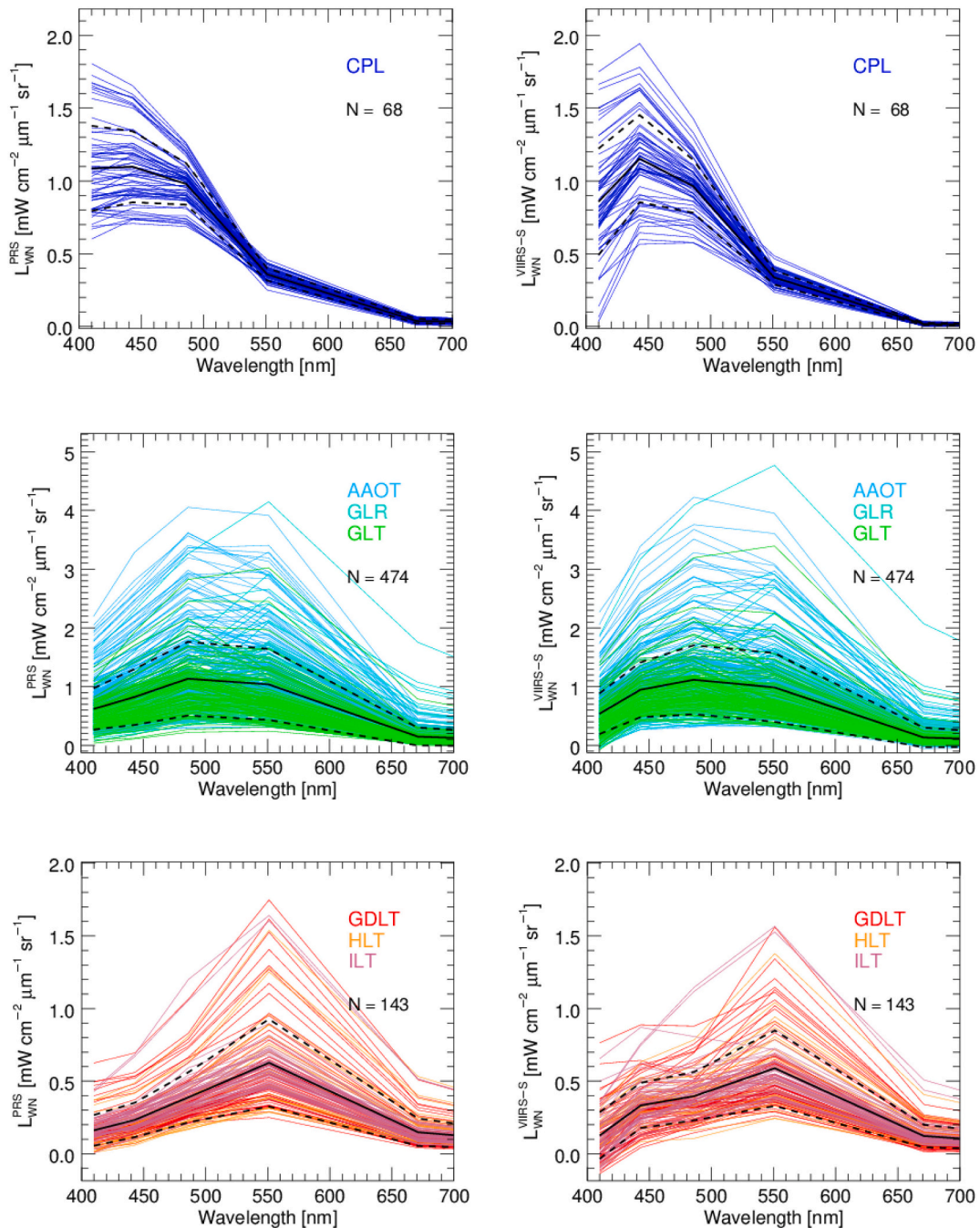
Fig. 9. AERONET-OC $L_{WN}^{PRS}(\lambda)$ and VIIRS-S $L_{WN}^{VIIRS-S}(\lambda)$ spectra, respectively, for different geographic water types (*i.e.*, oligotrophic-mesotrophic in the first row of panels; optically complex in the second row of panels; and optically complex, but dominated by high concentrations of CDOM in the last row of panels). The continuous black lines indicate median values while the dashed black lines indicate ±1 standard deviation.

approaching 0% across all center-wavelengths in the visible (see the left panel in Fig. 14). Conversely, results from the non-*Tandem Phase* show a much degraded agreement leading to spectrally averaged values of $\psi_m = -15\%$ (see the right panel in Fig. 14). More in detail, Table 6 shows values of ψ_m for the *Tandem Phase* generally within ±1% between 412 and 560 nm, +3% at 620 nm, +5% at 665 nm and −7% at 400 nm. Conversely, for the successive period, Table 7 shows values of ψ_m exhibiting large negative spectral biases varying between −14% and −41%, except at 510 and 560 nm where they show values of −9% and −5%, respectively. These large biases cannot be explained by the spatio-temporal mismatch between OLCI-A and OLCI-B. In fact, the ∼1 h systematic difference between the overpass of the sensors may only lead to random perturbations due to the bio-optical variability increasing the

dispersion of the data compared, while inaccuracy in the normalization of radiance data for the illumination conditions (which are a function of the sun zenith angle depending on the time of the day) and likely responsible for biases, should be negligible.

An evaluation of the viewing geometry characterizing the $L_{WN}^{OLCI-A}(\lambda)$ and $L_{WN}^{OLCI-B}(\lambda)$ matchups for the specific AAOT, GLR, GLT and ST7 locations, has shown distinct observation conditions with the OLCI-A and OLCI-B viewing angles exhibiting systematic differences with mean and standard deviations $\theta^{OLCI-A} = 8.4° \pm 6.9°$ and $\theta^{OLCI-B} = 48.4° \pm 7.0°$ (indicating that $\theta^{OLCI-A} \ll \theta^{OLCI-B}$ for the orbits characterizing the OLCI-A and OLCI-B matchups).

With reference to OLCI technology (Donlon et al., 2012) and the above values of θ^{OLCI-A} and θ^{OLCI-B}, the OLCI-A almost nadir viewing
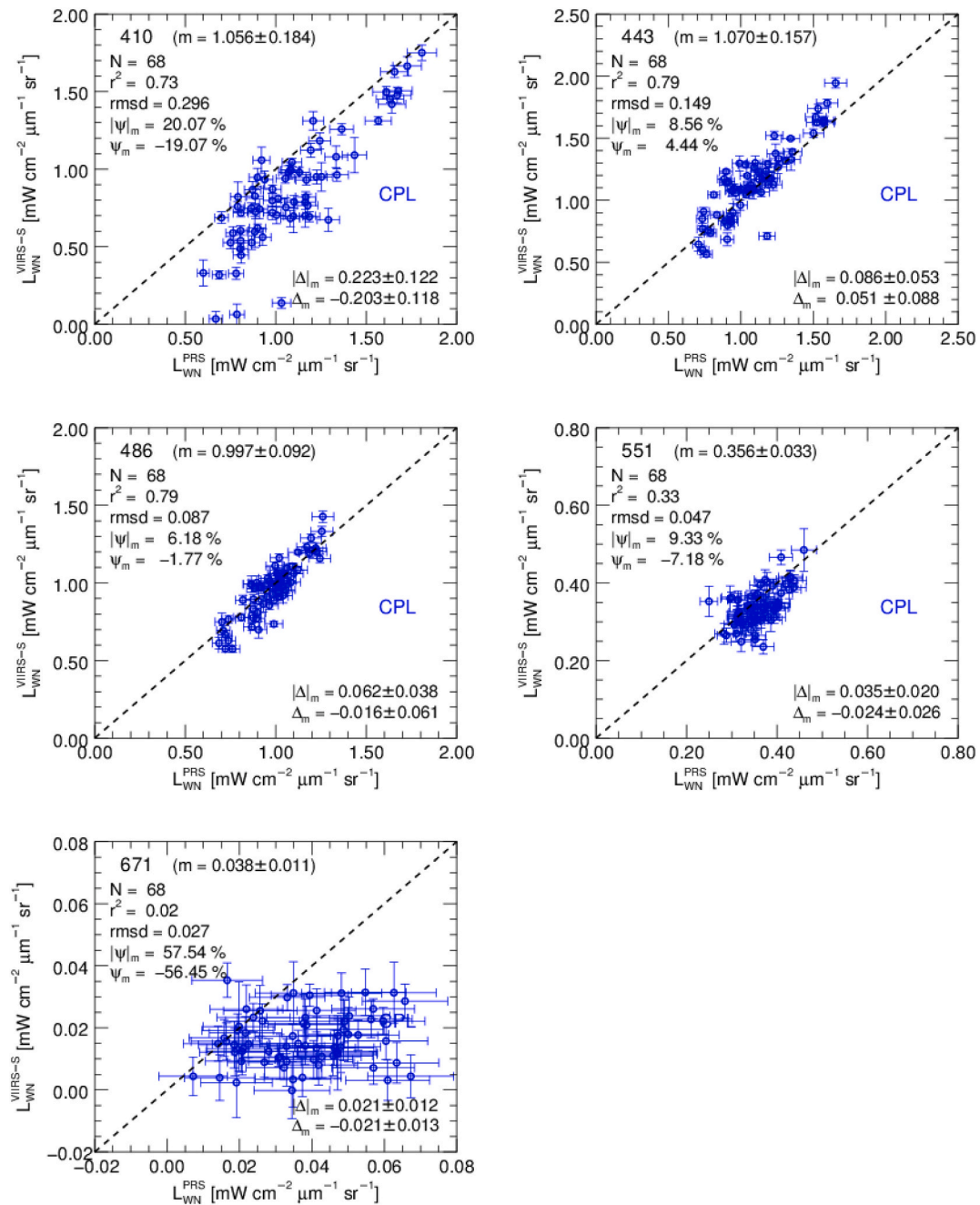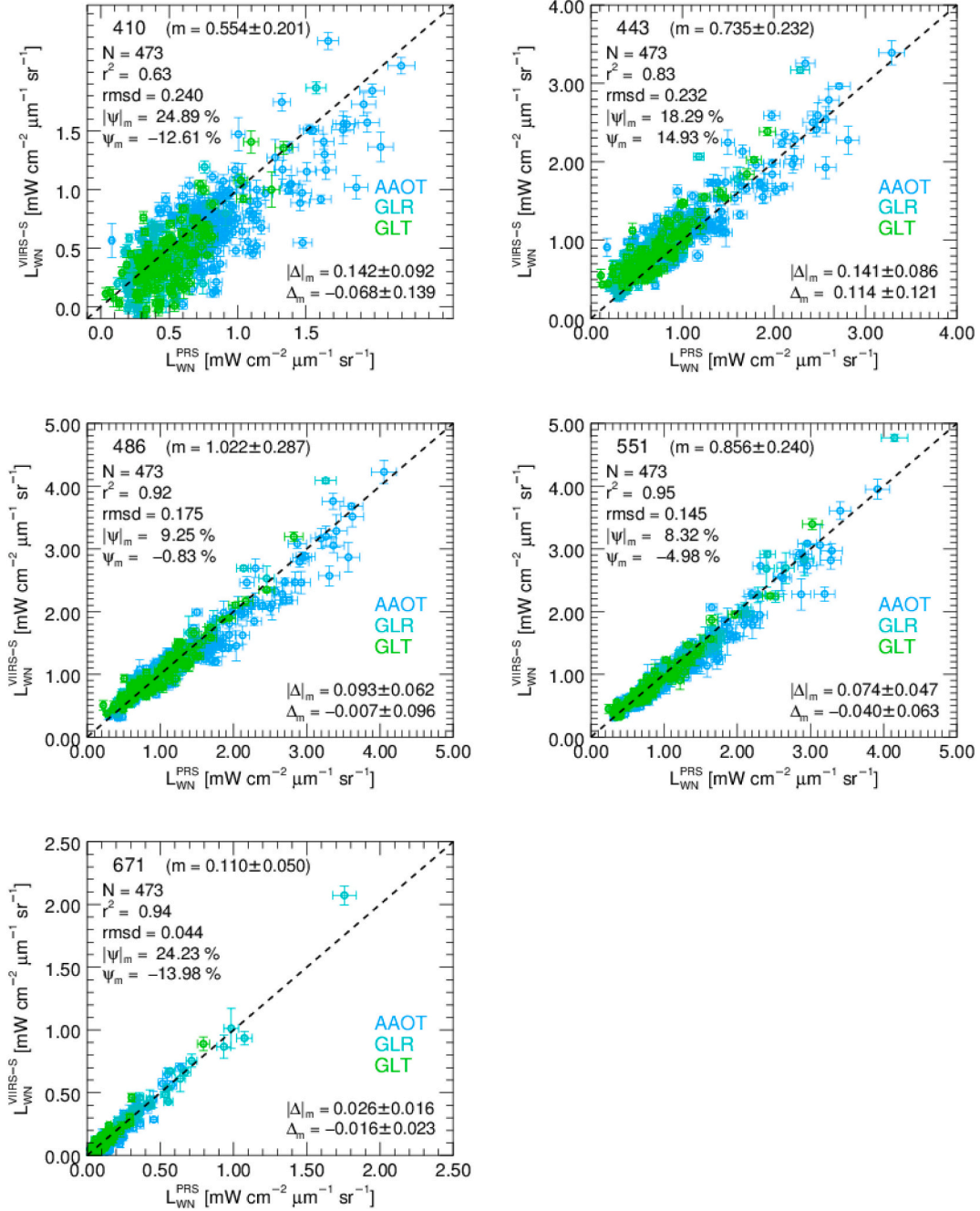
Fig. 10. Scatter plots of VIIRS-S $L_{WN}^{VIIRS-S}(\lambda)$ versus AERONET-OC $L_{WN}^{PRS}(\lambda)$ for oligotrophic-mesotrophic waters at the CPL site, at the 410, 443, 486, 551 and 671 nm center-wavelengths (with median and standard deviation of VIIRS-S viewing and sun zenith angles $\theta^{VIIRS-S} = 37.8° \pm 16.9°$ and $\theta_0 = 34.3° \pm 16.5°$, respectively). The error bars associated with the *in situ* data indicate measurement uncertainties while those related to satellite data indicate the variation coefficients determined from the 3×3 pixels contributing to matchups. N indicates the number of matchups, r^2 the determination coefficient, *rmsd* the root-mean square of differences, $|\psi|_m$ the median of unsigned percent differences, ψ_m the median of percent differences, $|\Delta|_m$ the median of unsigned differences and Δ_m the median of differences. The $\pm$ values associated with $|\Delta|_m$ and Δ_m are the median absolute deviations μ. The values in brackets aside the center-wavelength at the top of each panel, indicate the median $m \pm$ the related median absolute deviation μ of $L_{WN}^{PRS}(\lambda)$ at the specific center-wavelength λ.

geometry characterizing the comparison shown in Fig. 14 (see left panel) falls on cameras 3 and 4, while the OLCI-B viewing geometry falls on the westernmost camera 1. Excluding any systematic viewing angle dependence of the OLCI push-broom instruments, opposite to the angular response variations characterizing scanning radiometers such as VIIRS-S (see Barnes and Hu (2016)), the above finding suggests that the atmospheric correction process or alternatively inter-camera calibrations/characterizations are responsible for the observed viewing angle dependence. In fact, an inaccurate determination of the atmospheric path radiance, which exhibits larger values at high angles due to the

increase of scattering effects by atmospheric molecules and aerosols, would affect the atmospheric correction process as a function of the sensor viewing geometry. Also instrumental effects (*e.g.,* inter-camera calibrations and characterizations) cannot be definitively excluded. Nevertheless, they would lead to step-like discontinuities between cameras in the data products, which are currently unnoticed.

In view of further investigating the issue, a re-analysis of matchups for optically complex waters has been made by partitioning data as a function of the satellite viewing angles $\theta^{SAT} < 30°$ and $\theta^{SAT} \geq 30°$ (with *SAT* indicating either *OLCI-A, OLCI-B* or *VIIRS-S*). For OLCI-A and OLCI-
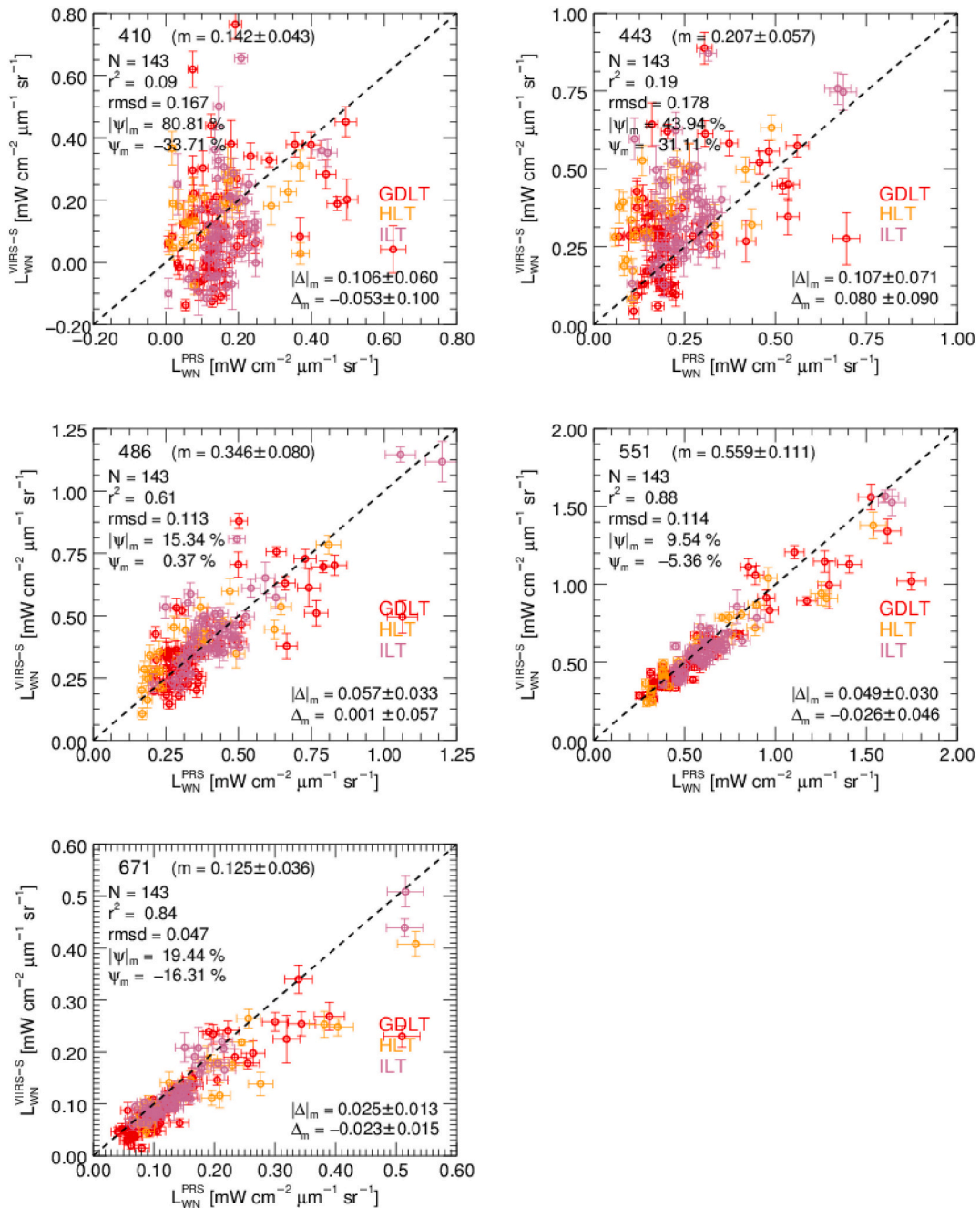
Fig. 11. Scatter plots of VIIRS-SNPP $L_{WN}^{VIIRS-S}(\lambda)$ versus AERONET-OC $L_{WN}^{PRS}(\lambda)$ as in Fig. 13, but for optically complex waters at the AAOT, GLR and GLT sites (with median and standard deviation of VIIRS-S viewing and sun zenith angles $\theta^{VIIRS-S} = 32.7° \pm 16.4°$ and $\theta_0 = 37.3° \pm 14.3°$, respectively).

B, the angles $\theta^{SAT} < 30°$ fall midway camera 2 and across cameras 3, 4 and 5. Conversely, $\theta^{SAT} \geq 30°$ fall onto camera 1 and midway camera 2. Results for OLCI-A, OLCI-B, and additionally for VIIRS-S, are summarized in Fig. 15 and ultimately confirm a negative trend of ψ_m with the viewing angle for both $L_{WN}^{OLCI-A}(\lambda)$ and $L_{WN}^{OLCI-B}(\lambda)$. In particular, both OLCI-A and OLCI-B matchups obtained with $\theta^{SAT} < 30°$ show spectrally averaged values of ψ_m close to -6% in the visible region, whereas the matchups obtained with $\theta^{SAT} \geq 30°$ exhibit spectrally average values of ψ_m approaching -16%. Conversely, VIIRS-S matchups do not exhibit any marked dependence on the viewing angle with spectrally averaged values of ψ_m close to -3% for $\theta^{VIIRS-S} < 30°$ and -4% for $\theta^{VIIRS-S} \geq 30°$. Detailed results on the former analysis are summarized in the *Annex* for each relevant center-wavelength.

A complementary evaluation of $\tau_a^{OLCI-A}(865)$ and α^{OLCI-A} has not

shown any significant difference between the statistical results from the data set partitioned as a function of the viewing angle, except for a slight change in the maximum of α^{OLCI-A} decreasing from 1.6 to 1.5.

The former findings on the viewing angle dependence of OCR data products could be, however, questioned due to the application of corrections for the bidirectional effects not specific for optically complex waters. Because of this, OLCI-A and OLCI-B data from the CPL site, which are expected to fully meet requirements for the application of $C_{f/Q}(\lambda)$ corrections, have also been evaluated by partitioning matchups according to θ^{SAT}. Results (not shown), confirm a negative trend with the increase of the viewing angle for both OLCI-A and OLCI-B. Specifically, spectrally averaged values of ψ_m close to $+4\%$ for $\theta^{OLCI-A} < 30°$ (N = 40, $\theta^{OLCI-A} = 17.2° \pm 7.2°$) and of -9% for $\theta^{OLCI-A} \geq 30°$ (N = 26, $\theta^{OLCI-A} = 42.9° \pm 7.1°$), have been determined for $L_{WN}^{OLCI-A}(\lambda)$. Results for

Fig. 12. Scatter plots of VIIRS-SNPP $L_{WN}^{VIIRS-S}(\lambda)$ versus AERONET-OC $L_{WN}^{PRS}(\lambda)$ as in Fig. 13, but for CDOM dominated waters at the GDLT, HLT and ILT sites (with median and standard deviation of VIIRS-S viewing and sun zenith angles $\theta^{VIIRS-S} = 29.1° \pm 15.9°$ and $\theta_0 = 39.3° \pm 5.3°$, respectively).

$L_{WN}^{OLCI-B}(\lambda)$ exhibit a less marked dependence, with spectrally averaged values of ψ_m close to $+2\%$ for $\theta^{OLCI-B} < 30°$ (N = 38, $\theta^{OLCI-B} = 16.1° \pm 6.0°$) and of -5% for $\theta^{OLCI-B} \geq 30°$ (N = 38, $\theta^{OLCI-B} = 44.7° \pm 6.7°$). It is noted, however, that the differences observed for OLCI-B with respect to OLCI-A at CPL could be explained by the relatively small number of matchups likely affecting the statistical representativity of data. It is also remarked that both $L_{WN}^{OLCI-A}(\lambda)$ and $L_{WN}^{OLCI-B}(\lambda)$ matchups exhibit better agreement with $L_{WN}^{PRS}(\lambda)$ in oligotrophic waters with respect to the optically complex water sites, which explains the smaller spectrally averaged values of ψ_m determined for the first with respect to the others.

The previous results and specifically the data provided in the *Annex* for both OLCI-A and OLCI-B, show negative spectral values of ψ_m largely increasing with the viewing angle from the red toward the blue center-

wavelengths. This supports a decreased performance of the atmospheric correction with the viewing angle as a result of an inaccurate determination of the atmospheric perturbations, which also increase from the red toward the blue due an increase of the atmospheric scattering. This outcome suggests a poor determination of the aerosol or even of the Rayleigh scattering contributions.

5. Summary and conclusions

Copernicus Sentinel-3A and -3B satellites, and the forthcoming Sentinel-3C and -3D, will ensure sustained and accessible ocean color data to support environmental and climate applications during the next two decades. This major space program entails actions to assess the fitness-for-purpose of data products. Within such a general framework,
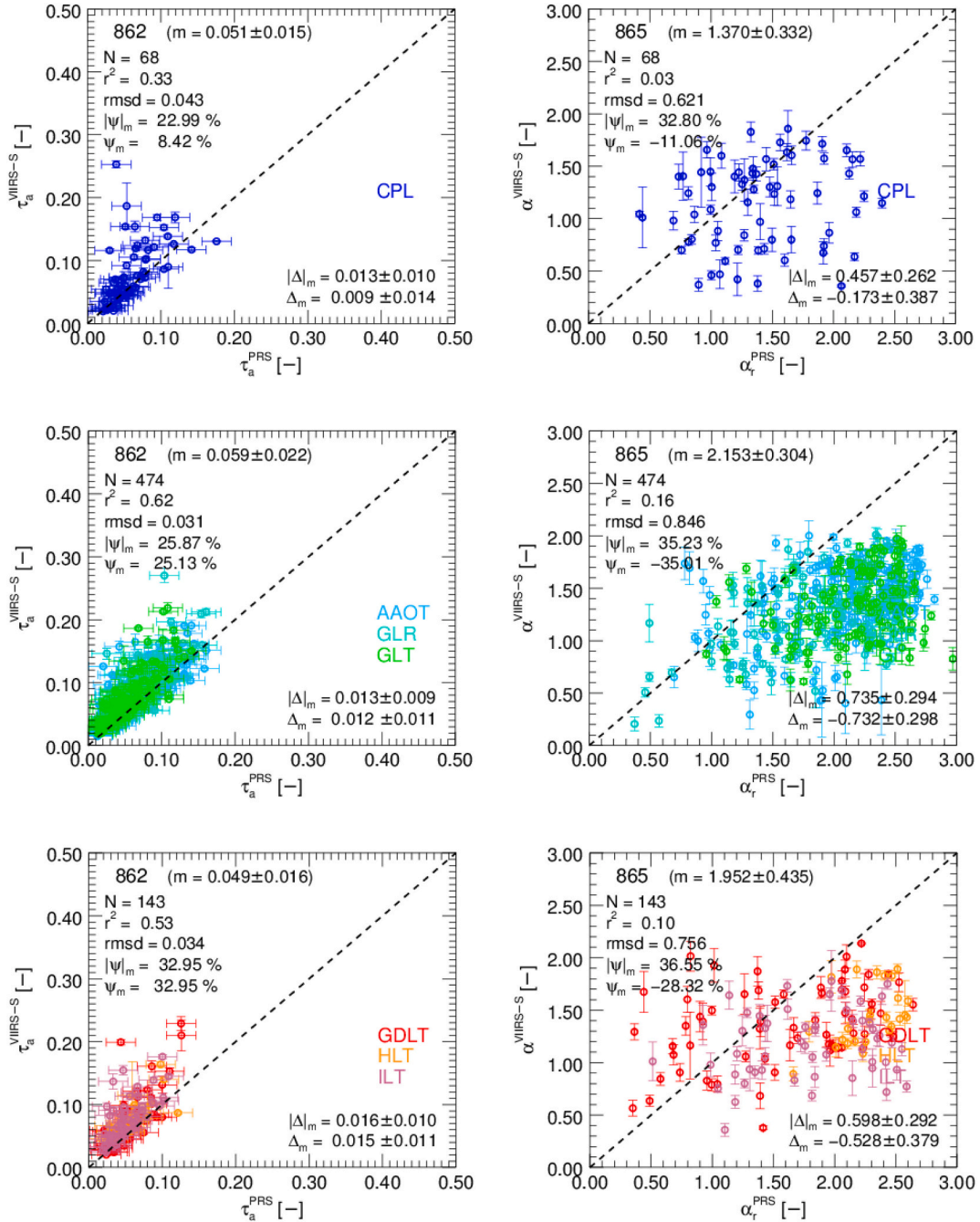
Fig. 13. Scatter plots of VIIR-S $\tau_a^{VIIRS-S}$(862) versus AERONET-OC τ_a^{PRS}(862) data (panels in the first column), and of $\alpha^{VIIRS-S}$ and α_r^{PRS} (panels in the second column). The panels in the various rows refer to different water types (*i.e.*, oligotrophic-mesotrophic waters in the first row of panels; optically complex waters in the second row of panels; and optically complex waters dominated by high concentrations of CDOM in the last row of panels). The error bars associated with the *in situ* data indicate measurement uncertainties while those related to satellite data indicate the variation coefficients determined from the 3×3 pixels contributing to matchups. N indicates the number of matchups, r^2 the determination coefficient, *rmsd* the root-mean square of differences, $|\psi|_m$ the median of unsigned percent differences, ψ_m the median of percent differences, $|\Delta|_m$ the median of unsigned differences and Δ_m the median of differences. The $\pm$ values associated with $|\Delta|_m$ and Δ_m are the median absolute deviations μ. The values in brackets aside the center-wavelength at the top of each panel, indicate the median $m \pm$ the related median absolute deviation μ of τ_a^{PRS}(862) and α_r^{PRS}.

the accuracy of fundamental data products from the Operational Baseline 3 Collection OL_L2M.003.01, have been investigated for OLCI-A and OLCI-B operated onboard Sentinel-3A and -3B, respectively.

The assessment of satellite derived normalized water-leaving radiance $L_{WN}(\lambda)$, aerosol optical depth $\tau_a(\lambda_n)$ in the near infrared and Ångström exponent α also determined in the near-infrared spectral region, has relied on matchups constructed using *in situ* reference data from AERONET-OC sites located in regions representative of diverse water

types: *i*. oligotrophic/mesotrophic waters; *ii*. generic optically complex waters characterized by different concentrations of suspended sediments and CDOM; and finally, *iii*. optically complex waters dominated by CDOM. Results indicate remarkable agreement of OLCI-A $L_{WN}^{OLCI-A}(\lambda)$ and OLCI-B $L_{WN}^{OLCI-B}(\lambda)$ with AERONET-OC $L_{WN}^{PRS}(\lambda)$ for oligotrophic/mesotrophic waters as documented by median percent differences ψ_m within approximately $\pm6\%$ at the blue-green center-wavelengths. However, an equivalent analysis performed for regions
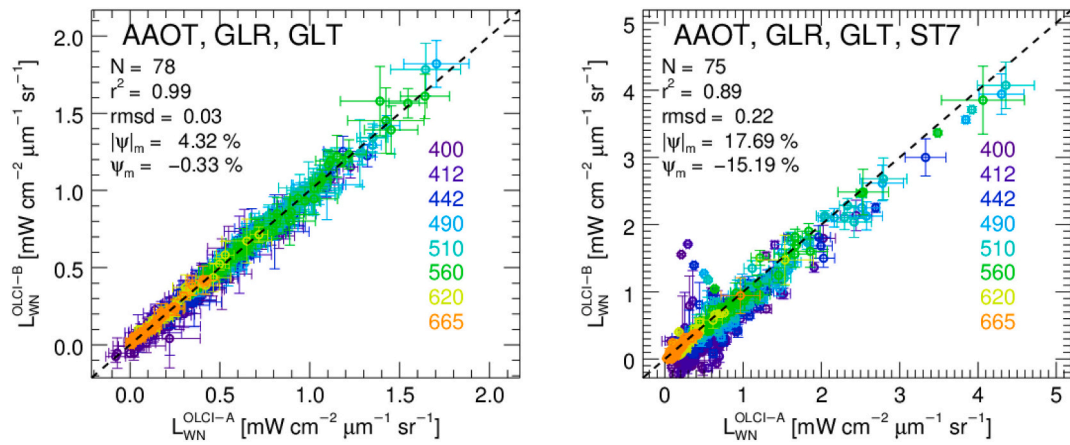
Fig. 14. Scatter plots of OLCI-B $L_{WN}^{OLCI-B}(\lambda)$ versus OLCI-A $L_{WN}^{OLCI-A}(\lambda)$ for optically complex waters at the AAOT, GLR, GLT and ST7 sites during the *Tandem* (left panel) and the *non-Tandem* (right panel) *Phases*. The error bars indicate the variation coefficients determined from the 3×3 pixels contributing to matchups. N indicates the number of matchups, r^2 the determination coefficient, *rmsd* the root-mean square of differences, $|\psi|_m$ the median of unsigned percent differences, ψ_m the median of percent differences. ST7 data were not available during the *Tandem Phase* because the specific AERONET-OC site was only established during August 2019.

Table 6
Summary results from OLCI-B $L_{WN}^{OLCI-B}(\lambda)$ and OLCI-A $L_{WN}^{OLCI-A}(\lambda)$ matchups analysis for the *Tandem Phase* over the optically complex waters at AAOT, GLR and GLT, at the 400, 412, 442, 490, 510, 560, 620 and 665 nm center-wavelengths.

	L_{WN}^{OLCI-B} vs L_{WN}^{OLCI-A}							
	N = 78, AAOT & GLR & GLT, $\tau_a^{OLCI-A}(870) = 0.136 \pm 0.060$, $\theta^{OLCI-A} = 31.5° \pm 15.4°$, $\theta^{OLCI-B} = 31.5° \pm 15.4°$, $\theta_0 = 39.8° \pm 8.4°$							
λ [nm]	**400**	**412**	**442**	**490**	**510**	**560**	**620**	**665**
$m \pm \mu$	0.299 ± 0.199	0.358 ± 0.217	0.522 ± 0.175	0.738 ± 0.183	0.736 ± 0.158	0.631 ± 0.146	0.122 ± 0.045	0.065 ± 0.028
$|\psi|_m$ [%]	9.21	7.07	4.38	2.87	2.29	1.97	6.20	8.38
ψ_m [%]	-6.87	-0.71	-1.87	-0.68	$+0.08$	$+0.39$	$+3.25$	$+4.74$
$|\Delta|_m \pm \mu$	0.030 ± 0.018	0.026 ± 0.014	0.023 ± 0.015	0.021 ± 0.012	0.018 ± 0.012	0.014 ± 0.010	0.009 ± 0.005	0.007 ± 0.004
$\Delta_m \pm \mu$	-0.026 ± 0.025	-0.003 ± 0.025	-0.007 ± 0.022	-0.004 ± 0.022	$+0.001 \pm 0.018$	$+0.002 \pm 0.013$	$+0.004 \pm 0.008$	$+0.003 \pm 0.005$
r^2 [−]	0.98	0.98	0.98	0.98	0.98	0.99	0.99	0.99
rmsd	0.050	0.040	0.038	0.033	0.030	0.035	0.017	0.011

N indicates the number of matchups, θ^{OLCI-A} and θ^{OLCI-B} the median $\pm$ the standard deviation of the satellite sensor viewing angle and θ_0 the median $\pm$ the standard deviation of the sun zenith. The symbol m indicates the median of $L_{WN}^{OLCI-A}(\lambda)$ at each center-wavelength λ, $|\psi|_m$ the median of unsigned percent differences, ψ_m the median of percent differences, $|\Delta|_m$ the median of unsigned differences, Δ_m the median of differences, r^2 the determination coefficient, *rmsd* the root-mean square of differences. The $\pm$ values associated with m, $|\Delta|_m$ and Δ_m are the median absolute deviations μ. When not specified, the quantities are in units of mW cm^{-2} μm^{-1} sr^{-1}.

Table 7
As in Table 6 but for the non-*Tandem Phase* for the optically complex waters at AAOT, GLR, GLT and ST7.

	L_{WN}^{OLCI-B} vs L_{WN}^{OLCI-A}							
	N = 75, AAOT & GLR & GLT & ST7, $\tau_a^{OLCI-A}(870) = 0.090 \pm 0.061$, $\theta^{OLCI-A} = 8.4° \pm 6.9°$, $\theta^{OLCI-B} = 48.4° \pm 7.0°$, $\theta_0 = 47.7° \pm 11.7°$							
λ [nm]	**400**	**412**	**442**	**490**	**510**	**560**	**620**	**665**
$m \pm \mu$	0.479 ± 0.184	0.593 ± 0.215	0.692 ± 0.228	0.787 ± 0.232	0.755 ± 0.202	0.657 ± 0.187	0.154 ± 0.053	0.088 ± 0.031
$|\psi|_m$ [%]	55.19	47.89	29.14	16.09	11.49	6.71	18.92	20.83
ψ_m [%]	-40.92	-37.73	-25.48	-13.55	-9.00	-4.74	-15.01	-17.02
$|\Delta|_m \pm \mu$	0.239 ± 0.118	0.293 ± 0.116	0.209 ± 0.096	0.147 ± 0.068	0.093 ± 0.050	0.051 ± 0.034	0.031 ± 0.021	0.023 ± 0.015
$\Delta_m \pm \mu$	-0.222 ± 0.127	-0.238 ± 0.120	-0.177 ± 0.098	-0.132 ± 0.068	-0.080 ± 0.060	-0.036 ± 0.044	-0.027 ± 0.023	-0.017 ± 0.015
r^2 [−]	0.54	0.61	0.83	0.95	0.96	0.98	0.95	0.94
rmsd	0.348	0.353	0.275	0.205	0.160	0.105	0.054	0.037

characterized by generic optically complex waters shows degraded results. Further degraded results are observed for CDOM dominated waters with negative values of $L_{WN}^{OLCI-A}(\lambda)$ and $L_{WN}^{OLCI-B}(\lambda)$ in the blue spectral region likely explained by inaccuracies introduced by the atmospheric correction, enhanced by the very low water-leaving radiance values approaching zero in the blue spectral region. The observed accuracy of $L_{WN}^{OLCI-A}(\lambda)$ and $L_{WN}^{OLCI-B}(\lambda)$ decreasing with an increase of the optical complexity of water, is unlikely explained by diverse factors such as the illumination and sensor viewing geometries characterizing the different geographic regions. In fact, the matchups investigated in this study, mostly exhibit close median values for the sun zenith and also of the satellite viewing angles, regardless of the water type.

Overall results from this study, indicate that the spectral inconsistencies affecting $L_{WN}^{OLCI-A}(\lambda)$ together with the major positive biases affecting $L_{WN}^{OLCI-B}(\lambda)$ in the Operational Baseline Collection 2 products, are now largely solved due to the determination and application of cross-mission consistent SVC adjustment factors. Additionally, the unique opportunity offered by the *Tandem Phase* for a direct comparison of $L_{WN}^{OLCI-A}(\lambda)$ and $L_{WN}^{OLCI-B}(\lambda)$ indicates outstanding agreement with spectrally averaged values of ψ_m approaching 0% across the center-wavelengths in the visible, and with spectral values of ψ_m within -2% and 0% in the 412–560 nm spectral range, and of $+3\%$, $+5\%$ and -7% at 620, 665, and 400 nm, respectively, across generic optically complex waters. These results well support the cross-mission
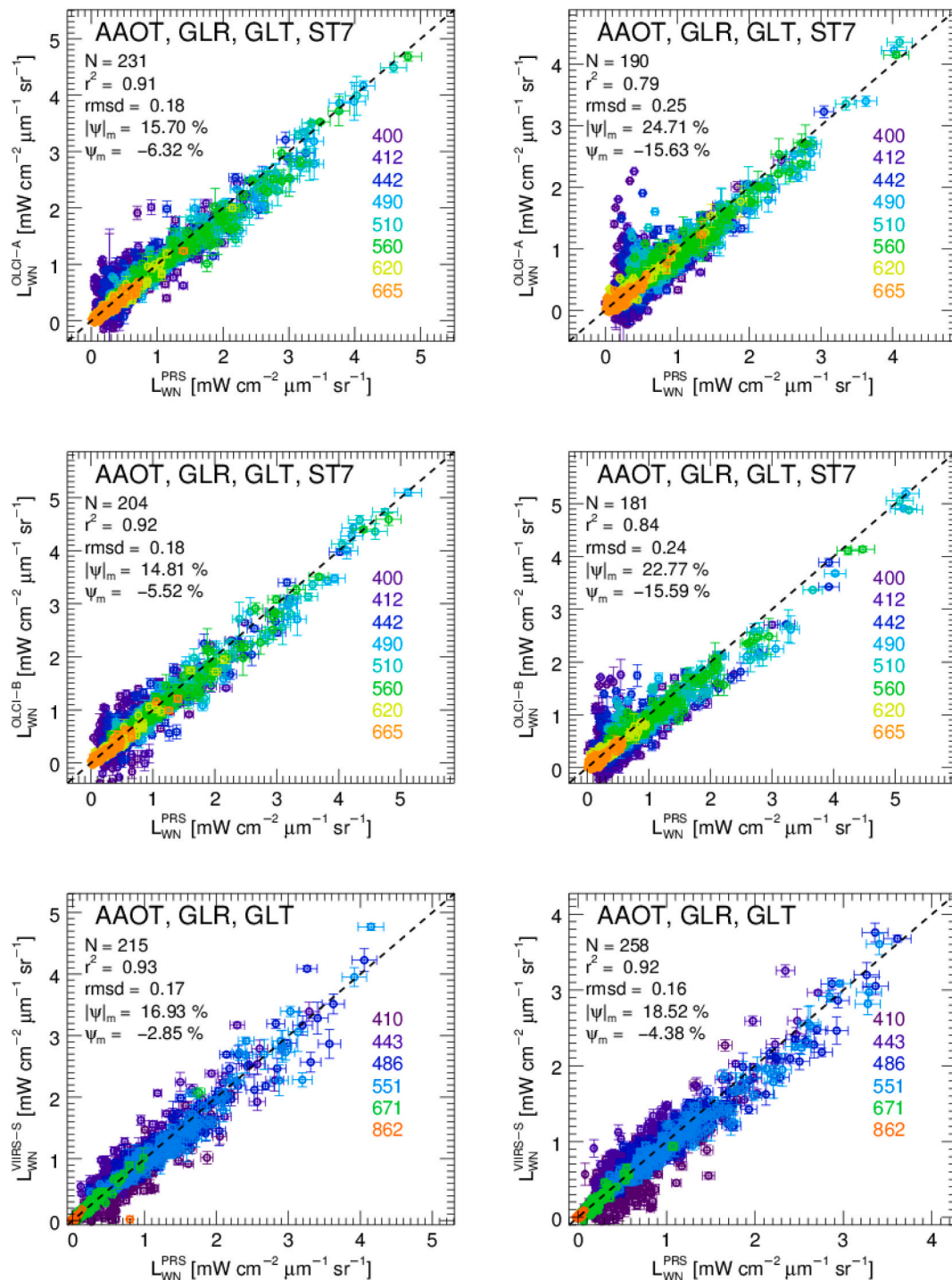
Fig. 15. Scatter plots of OLCI-A $L_{WN}^{OLCI-A}(\lambda)$, OLCI-B $L_{WN}^{OLCI-B}(\lambda)$ and VIIRS-S $L_{WN}^{VIIRS-S}(\lambda)$ versus AERONET-OC $L_{WN}^{PRS}(\lambda)$ for the optically complex sites partitioned according to $\theta^{SAT} < 30°$ (left panels) and $\theta^{SAT} \geq 30°$ (right panels) with SAT indicating OLCI-A, OLCI-B or VIIRS-S. The error bars indicate the variation coefficients determined from the 3×3 pixels contributing to matchups. N indicates the number of matchups, r^2 the determination coefficient, *rmsd* the root-mean square of differences, $|\psi|_m$ the median of unsigned percent differences, ψ_m the median of percent differences.

consistency of OLCI-A and OLCI-B data products. However, OLCI-A and OLCI-B matchup analyses restricted to simultaneous observations of the same AERONET-OC locations, show large differences outside the *Tandem Phase* with spectrally averaged values of ψ_m of -15% across the center-wavelengths in the visible region. These variations have been related to systematic differences in the viewing geometry, confirmed by a re-analysis of OLCI-A and OLCI-B matchups partitioned as a function of the viewing angle. This finding suggests a dependence of the atmospheric correction on the viewing angle, even though some contribution

from the characterization and calibration of the various OLCI cameras cannot be excluded.

Results from the analysis of $\tau_a^{OLCI-A}(865)$, $\tau_a^{OLCI-B}(865)$, α^{OLCI-A} and α^{OLCI-B} by-products across different geographic regions exhibit overestimated values between $+48\%$ and $+79\%$ for the aerosol optical depth and underestimated values between -28% and -41% for the Ångström exponent. Additionally, both α^{OLCI-A} and α^{OLCI-B} show values not exceeding approximately 1.6 while the *in situ* one vary up to 3.0. This may suggest difficulties in the identification of the aerosol types with

potential implications on the accuracy of the atmospheric correction process.

The analysis of VIIRS-S matchups relying on AERONET-OC data, proposed as a further term of reference for OLCI-A and OLCI-B data products in view of creating Climate Data Records through the combination of these independent data products, led to peculiar findings. Specifically, the assessment results suggest spectral inconsistencies of $L_{WN}^{VIIRS-S}(\lambda)$ in the blue spectral region with underestimates at 410 nm documented by $\psi_m = -16\%$ and conversely overestimates at 443 nm indicated by $\psi_m = +9\%$ over optically complex waters. Largely underestimated values of $L_{WN}^{VIIRS-S}(\lambda)$ are also observed at 671 nm. Opposite to OLCI-A and OLCI-B data products, VIIRS-S data do not show any large or systematic dependence on water type and satellite viewing angle at the 486 and 551 nm key center-wavelengths. Similar to OLCI-A and OLCI-B by-products from the atmospheric correction, $\tau_a^{VIIRS-S}(862)$ exhibits overestimates, but with values of ψ_m restricted in the range of $+8\%$ to $+33\%$. Finally, $\alpha^{VIIRS-S}$, that exhibits values up to 2, also shows underestimates with ψ_m varying between -11% and -35% across the various water types.

All the above results further underline that diverse atmospheric corrections may lead to largely different product accuracies, regardless of the implementation of equivalent SVC schemes (as it is for VIIRS-S, OLCI-A and OLCI-B). This emphasizes the need for standardizing the atmospheric correction across the various ocean color missions benefitting of identical models well representing actual aerosol types.

The current study has also further shown the need for a high statistical representativity of matchups in a variety of validation sites to avoid results biased by restricted measurement conditions. Moreover, in addition to the presentation of statistical results from the validation exercise, the provision of any relevant information qualifying the measurements and the measurement conditions, is essential. This would at least help indicating when results from independent studies can be intercompared.

Declaration of Competing Interest

Acknowledgments

Annex A: Results from the matchups analysis as a function of the satellite sensor viewing angle.

Tables A1 through A6 show detailed results from the analysis of data products in optically complex waters performed by partitioning matchups according to the values of the sensor viewing angle $\theta^{SAT} < 30°$ and $\theta^{SAT} \geq 30°$ (with *SAT* indicating OLCI-A, OLCI-B or VIIRS-S).

Results summarized in Tables A1 and A2 for OLCI-A indicate a large dependence of $L_{WN}^{OLCI-A}(\lambda)$ on the viewing angle. In particular, while matchups obtained with $\theta^{OLCI-A} < 30°$ show values of ψ_m within $\pm 6\%$ in the 400–560 nm spectral region, matchups obtained with $\theta^{OLCI-A} \geq 30°$ exhibit values of ψ_m varying between -9% and -30%. Results from an equivalent analysis presented in Tables A3 and A4 for OLCI-B shows values of ψ_m consistent with those obtained for OLCI-A. Specifically, matchups obtained with $\theta^{OLCI-B} < 30°$ show values of ψ_m within $\pm 5\%$ in the 400–560 nm spectral region, while matchups obtained with $\theta^{OLCI-B} \geq 30°$ exhibit values of ψ_m varying between -7% and -26%.

Results summarized in Tables A5 and A6 for VIIRS-S do not indicate any large dependence of $L_{WN}^{VIIRS-S}(\lambda)$ on the viewing angle with differences between the ψ_m values determined from the partitioned matchups generally agreeing within $\pm 2\%$, excluding the center-wavelength at 671 nm (-10% for $\theta^{VIIRS-S} \geq 30°$ with respect to $\theta^{VIIRS-S} < 30°$).

Table A1
Summary results from OLCI-A $L_{WN}^{OLCI-A}(\lambda)$ and AERONET-OC $L_{WN}^{PRS}(\lambda)$ matchups analysis for the optically complex waters at AAOT, GLR, GLT and ST7, with the satellite viewing angle $\theta^{OLCI-A} < 30°$, at the 400, 412, 442, 490, 510, 560, 620 and 665 nm center-wavelengths.

				L_{WN}^{OLCI-A} vs L_{WN}^{PRS} $N = 231$, AAOT & GLR & GLT & ST7, $\tau_a^{PRS}(870) = 0.062\pm0.043$, $\theta^{OLCI-A} = 14.6°\pm8.6°$, $\theta_0 = 43.5°\pm12.4°$				
λ [nm]	**400**	**412**	**442**	**490**	**510**	**560**	**620**	**665**
$m \pm \mu$	0.366±0.148	0.481±0.184	0.623±0.215	0.863±0.263	0.841±0.248	0.702±0.223	0.165±0.076	0.100±0.047
$|\psi|_m$ [%]	33.15	26.20	18.21	10.94	9.06	9.12	19.44	25.93
ψ_m [%]	+5.62	+0.52	+0.47	−4.05	−3.04	−5.83	−11.98	−20.77
$|\Delta|_m \pm \mu$	0.143±0.082	0.147±0.089	0.120±0.074	0.094±0.057	0.085±0.053	0.067±0.042	0.031±0.021	0.028±0.018
$\Delta_m \pm \mu$	+0.016±0.148	+0.006±0.148	+0.002±0.121	−0.041±0.102	−0.028±0.078	−0.045±0.060	−0.021±0.031	−0.025±0.023
r^2 [−]	0.54	0.66	0.86	0.95	0.96	0.97	0.95	0.93
$rmsd$	0.271	0.264	0.213	0.171	0.158	0.146	0.067	0.053

N indicates the number of matchups, θ^{OLCI-A} the median $\pm$ the standard deviation of the satellite sensor viewing angle and θ_0 the median $\pm$ the standard deviation of the sun zenith. The symbol m indicates the median of $L_{WN}^{PRS}(\lambda)$ at each center-wavelength λ, $|\psi|_m$ the median of unsigned percent differences, ψ_m the median of percent differences, $|\Delta|_m$ the median of unsigned differences, Δ_m the median of differences, r^2 the determination coefficient, *rmsd* the root-mean square of differences. The $\pm$ values associated with m, $|\Delta|_m$ and Δ_m are the median absolute deviations μ. When not specified, the quantities are in units of mW cm^{-2} μm^{-1} sr^{-1}.

Table A2
As in A1 but with $\theta^{OLCI-A} \geq 30°$.

| | | | | L_{WN}^{OLCI-A} vs L_{WN}^{PRS} | | | | |
| | | | $N = 190$, AAOT & GLR & GLT & ST7, $\tau_a^{PRS}(870) = 0.061 \pm 0.041$, $\theta^{OLCI-A} = 43.5° \pm 7.2°$, $\theta_0 = 41.5° \pm 11.4°$ | | | | |
λ [nm]	**400**	**412**	**442**	**490**	**510**	**560**	**620**	**665**
$m \pm \mu$	0.339±0.119	0.424±0.145	0.558±0.182	0.775±0.249	0.802±0.248	0.716±0.257	0.179±0.086	0.107±0.049
$\|\psi\|_m$ [%]	55.08	48.08	29.14	18.42	14.15	12.31	27.36	36.53
ψ_m [%]	−29.89	−26.27	−14.00	−13.44	−9.91	−8.91	−20.57	−31.38
$\|\Delta\|_m \pm \mu$	0.211±0.102	0.238±0.125	0.175±0.095	0.174±0.089	0.136±0.072	0.100±0.057	0.058±0.033	0.047±0.023
$\Delta_m \pm \mu$	−0.119±0.172	−0.131±0.187	−0.098±0.145	−0.121±0.098	−0.082±0.092	−0.069±0.072	−0.044±0.039	−0.040±0.028
r^2 [−]	0.21	0.29	0.62	0.86	0.89	0.94	0.90	0.88
$rmsd$	0.364	0.382	0.297	0.238	0.198	0.151	0.086	0.067

Table A3
Summary results from OLCI-B $L_{WN}^{OLCI-B}(\lambda)$ and AERONET-OC $L_{WN}^{PRS}(\lambda)$ matchups analysis for the optically complex waters at AAOT, GLR, GLT and ST7, with the satellite viewing angle $\theta^{OLCI-B} < 30°$, at the 400, 412, 442, 490, 510, 560, 620 and 665 nm center-wavelengths.

| | | | | L_{WN}^{OLCI-B} vs L_{WN}^{PRS} | | | | |
| | | | $N = 204$, AAOT & GLR & GLT & ST7, $\tau_a^{PRS}(870) = 0.062 \pm 0.024$, $\theta^{OLCI-B} = 14.2° \pm 7.4°$, $\theta_0 = 42.9° \pm 9.5°$ | | | | |
λ [nm]	**400**	**412**	**442**	**490**	**510**	**560**	**620**	**665**
$m \pm \mu$	0.357±0.129	0.454±0.169	0.586±0.202	0.827±0.256	0.835±0.234	0.722±0.226	0.160±0.072	0.097±0.044
$\|\psi\|_m$ [%]	36.38	28.96	17.31	10.73	9.31	8.88	17.93	26.93
ψ_m [%]	+5.17	−0.51	+1.60	−4.70	−3.26	−4.63	−9.71	−21.13
$\|\Delta\|_m \pm \mu$	0.147±0.102	0.152±0.095	0.116±0.078	0.091±0.057	0.078±0.047	0.066±0.040	0.031±0.023	0.029±0.017
$\Delta_m \pm \mu$	+0.031±0.162	−0.002±0.149	+0.006±0.117	−0.040±0.085	−0.026±0.070	−0.042±0.054	−0.018±0.029	−0.024±0.021
r^2 [−]	0.53	0.66	0.86	0.96	0.97	0.98	0.96	0.94
$rmsd$	0.273	0.268	0.218	0.168	0.143	0.125	0.065	0.054

N indicates the number of matchups, θ^{OLCI-B} the median ± the standard deviation of the satellite sensor viewing angle and θ_0 the median ± the standard deviation of the sun zenith. The symbol m indicates the median of $L_{WN}^{PRS}(\lambda)$ at each center-wavelength λ, $\|\psi\|_m$ the median of unsigned percent differences, ψ_m the median of percent differences, $\|\Delta\|_m$ the median of unsigned differences, Δ_m the median of differences, r^2 the determination coefficient, $rmsd$ the root-mean square of differences. The ± values associated with m, $\|\Delta\|_m$ and Δ_m are the median absolute deviations μ. When not specified, the quantities are in units of mW cm^{-2} μm^{-1} sr^{-1}.

Table A4
As in A3 but with $\theta^{OLCI-B} \geq 30°$.

| | | | | L_{WN}^{OLCI-B} vs L_{WN}^{PRS} | | | | |
| | | | $N = 181$, AAOT & GLR & GLT & ST7, $\tau_a^{PRS}(870) = 0.068 \pm 0.024$, $\theta^{OLCI-B} = 42.7° \pm 6.1°$, $\theta_0 = 42.3° \pm 8.0°$ | | | | |
λ [nm]	**400**	**412**	**442**	**490**	**510**	**560**	**620**	**665**
$m \pm \mu$	0.359±0.135	0.460±0.170	0.561±0.181	0.824±0.245	0.811±0.228	0.760±0.217	0.183±0.078	0.110±0.050
$\|\psi\|_m$ [%]	55.96	46.51	28.66	16.99	13.31	12.05	25.28	37.49
ψ_m [%]	−26.07	−23.42	−14.06	−12.62	−7.42	−9.42	−19.78	−33.42
$\|\Delta\|_m \pm \mu$	0.237±0.114	0.230±0.112	0.171±0.081	0.136±0.090	0.109±0.072	0.102±0.059	0.051±0.031	0.046±0.023
$\Delta_m \pm \mu$	−0.121±0.169	−0.132±0.166	−0.102±0.140	−0.105±0.102	−0.064±0.101	−0.075±0.070	−0.039±0.035	−0.041±0.027
r^2 [−]	0.30	0.42	0.73	0.91	0.93	0.95	0.86	0.80
$rmsd$	0.344	0.358	0.286	0.228	0.201	0.162	0.077	0.065

Table A5
Summary results from VIIRS-S $L_{WN}^{VIIRS-S}(\lambda)$ and AERONET-OC $L_{WN}^{PRS}(\lambda)$ matchups analysis with satellite viewing angle $\theta^{VIIRS-S} < 30°$ for the optically complex waters at AAOT, GLR and GLT, at the 410, 443, 486, 551, and 671 nm center-wavelengths.

| | | $L_{WN}^{VIIRS-N}$ vs L_{WN}^{PRS} | | |
| | $N = 215$, AAOT & GLR & GLT, $\tau_a^{PRS}(862) = 0.056 \pm 0.034$, $\theta^{VIIRS-N} = 15.9° \pm 8.9°$, $\theta_0 = 40.9° \pm 14.6°$ | | | |
λ [nm]	**410**	**443**	**486**	**551**	**671**
$m \pm \mu$	0.596±0.218	0.777±0.258	1.049±0.332	0.897±0.293	0.117±0.055
$\|\psi\|_m$ [%]	22.72	18.11	8.90	7.99	20.75
ψ_m [%]	−11.53	+13.37	+0.03	−4.31	−10.81
$\|\Delta\|_m \pm \mu$	0.125±0.087	0.137±0.087	0.100±0.062	0.076±0.048	0.025±0.015
$\Delta_m \pm \mu$	−0.064±0.134	+0.106±0.119	+0.000±0.101	−0.037±0.066	−0.012±0.024
r^2 [−]	0.67	0.83	0.92	0.95	0.96
$rmsd$	0.235	0.243	0.190	0.161	0.046

N indicates the number of matchups, $\theta^{VIIRS-N}$ the median ± the standard deviation of the satellite sensor viewing angle and θ_0 the median ± the standard deviation of the sun zenith. The symbol m indicates the median and the related median absolute deviation of $L_{WN}^{PRS}(\lambda)$ at each center-wavelength λ, $\|\psi\|_m$ the median of unsigned percent differences, ψ_m the median of percent differences, $\|\Delta\|_m$ the median of unsigned differences, Δ_m the median of differences, r^2 the determination coefficient, $rmsd$ the root-mean square of differences. The ± values associated with m, $\|\Delta\|_m$ and Δ_m are the median absolute deviations μ. When not specified, the quantities are in units of mW cm^{-2} μm^{-1} sr^{-1}.

Table A6

As in Table A5 but with $\theta^{VIIRS-N} \geq 30°$.

	$L_{WN}^{VIIRS-N}$ vs L_{WN}^{PRS} $N = 258$, AAOT & GLR & GLT, $\tau_a^{PRS}(862) = 0.060 \pm 0.030$, $\theta^{VIIRS-N} = 43.7° \pm 8.1°$, $\theta_0 = 33.3° \pm 13.7°$				
λ [nm]	410	443	486	551	671
$m \pm \mu$	0.518 ± 0.189	0.705 ± 0.216	0.972 ± 0.265	0.812 ± 0.205	0.099 ± 0.043
$|\psi|_m$ [%]	28.22	18.49	9.78	8.56	28.50
ψ_m [%]	-13.55	$+16.08$	-1.17	-5.25	-20.50
$|\Delta|_m \pm \mu$	0.147 ± 0.090	0.143 ± 0.087	0.090 ± 0.063	0.074 ± 0.046	0.030 ± 0.017
$\Delta_m \pm \mu$	-0.069 ± 0.143	$+0.117 \pm 0.121$	-0.010 ± 0.090	$+0.044 \pm 0.063$	-0.020 ± 0.024
r^2 [$-$]	0.57	0.82	0.92	0.95	0.90
$rmsd$	0.244	0.224	0.162	0.131	0.043

References

Ahmad, Z., Franz, B.A., McClain, C.R., Kwiatkowska, E.J., Werdell, J., Shettle, E.P., Holben, B.N., 2010. New aerosol models for the retrieval of aerosol optical thickness and normalized water-leaving radiances from the SeaWiFS and MODIS sensors over coastal regions and open oceans. Appl. Opt. 49, 5545–5560. https://doi.org/10.1364/AO.49.005545.

Antoine, D., Morel, A., 1999. A multiple scattering algorithm for atmospheric correction of remotely sensed ocean color (MERIS instrument): principle and implementation for atmospheres carrying various aerosols including absorbing ones. Int. J. Remote Sens. 20 (9), 1875–1916.

Barnes, B.B., Hu, C., 2016. Dependence of satellite ocean color data products on viewing angles: A comparison between SeaWiFS, MODIS, and VIIRS. Remote Sens. Environ. 175, 120–129.

Behrenfeld, M.J., O'Malley, R.T., Siegel, D.A., McClain, C.R., Sarmiento, J.L., Feldman, G.C., Milligan, A.J., Falkowski, P.G., Letelier, R.M., Boss, E.S., 2006. Climate-driven trends in contemporary ocean productivity. Nature 444, 752–755. https://doi.org/10.1038/nature05317.

Berthon, J.F., Mélin, F., Zibordi, G., 2008. Ocean colour remote sensing of the optically complex European seas. In: Remote Sensing of the European Seas. Springer, Dordrecht, pp. 35–52.

Bezy, J.-L., Delwart, S., Rast, M., 2000. MERIS - a new generation of ocean-colour sensor onboard Envisat. ESA Bull. 103, 48–56.

Cazzaniga, I., Zibordi, G., Mélin, F., 2021. Spectral variations of the remote sensing reflectance during coccolithophore blooms in the Western Black Sea. Remote Sens. Environ. 264, 112607.

Clerc, S., Donlon, C., Borde, F., Lamquin, N., Hunt, S.E., Smith, D., Mcmillan, M., Mittaz, J., Woolliams, E., Hammond, M., Banks, C., Moreau, T., Picard, B., Raynal, M., Rieu, P., Guerou, A., 2020. Benefits and Lessons Learned from the Sentinel-3 Tandem Phase. Remote Sens. 12, 2668. https://doi.org/10.3390/rs12172668.

Donlon, C., Berruti, B., Buongiorno, A., Ferreira, M.-H., Féménias, P., Frerick, J., Goryl, P., Klein, U., Laur, H., Mavrocordatos, C., Nieke, J., Rebhan, H., Seitz, B., Stroede, J., Sciarra, R., 2012. The global monitoring for environment and security (GMES) Sentinel-3 mission. Remote Sens. Environ. 120, 37–57. https://doi.org/10.1016/j.rse.2011.07.024.

Eplee, R.E., Meister, G., Patt, F.S., Barnes, R.A., Bailey, S.W., Franz, B.A., McClain, C.R., 2012. On-orbit calibration of SeaWiFS. Appl. Opt. 51, 8702–8730.

Esaias, W.E., Abbott, M.R., Barton, I., Brown, O.B., Campbell, J.W., Carder, K.L., Clark, D.K., Evans, R.H., Hoge, F.E., Gordon, H.R., Balch, W.M., Letelier, R., Minnett, P.J., 1998. An overview of MODIS capabilities for ocean science observations. IEEE Trans. Geosci. Remote Sens. 36, 1250–1265. https://doi.org/10.1109/36.701076.

Franz, B.A., Bailey, S.W., Werdell, P.J., McClain, C.R., 2007. Sensor-independent approach to the vicarious calibration of satellite ocean color radiometry. Appl. Opt. 46, 5068–5082. https://doi.org/10.1364/AO.46.005068.

Frouin, R., Schwindling, M., Deschamps, P.Y., 1996. Spectral reflectance of sea foam in the visible and near-infrared: In situ measurements and remote sensing implications. J. Geophys. Res. C Ocean. 101, 14361–14371. https://doi.org/10.1029/96JC00629.

Gergely, M., Zibordi, G., 2014. Assessment of AERONET-OC L WN uncertainties. Metrologia 51, 40–47. https://doi.org/10.1088/0026-1394/51/1/40.

Goldberg, M.D., Kilcoyne, H., Cikanek, H., Mehta, A., 2013. Joint Polar Satellite System: The United States next generation civilian polar-orbiting environmental satellite system. J. Geophys. Res. Atmos. 118, 13413–463475. https://doi.org/10.1002/2013JD020389.

Holben, B.N., Eck, T.F., Slutsker, I., Tanré, D., Buis, J.P., Setzer, A., Vermote, E., Reagan, J.A., Kaufman, Y.J., Nakajima, T., Lavenu, F., Jankowiak, I., Smirnov, A., 1998. AERONET - a federated instrument network and data archive for aerosol characterization. Remote Sens. Environ. 66, 1–16. https://doi.org/10.1007/BF03174421.

Holben, B.N., Tanré, D., Smirnov, A., Eck, T.F., Slutsker, I., Abuhassan, N., Newcomb, W. W., Schafer, J.S., Chatenet, B., Lavenu, F., Kaufman, Y.J., Vande Castle, J., Setzer, A., Markham, B., Clark, D., Frouin, R., Halthore, R., Karneli, A., O'Neill, N.T., Pietras, C., Pinker, R.T., Voss, K., Zibordi, G., 2001. An emerging ground-based aerosol climatology: Aerosol optical depth from AERONET. J. Geophys. Res. 106, 12067–12097. https://doi.org/10.1029/2001JD900014.

IOCCG, 2010. Atmospheric correction for remotely-sensed ocean-colour products. In: Wang, M. (Ed.), Reports of the International Ocean-Colour Coordinating Group, vol. N. 10. IOCCG, Dartmouth, Canada.

Koepke, P., 1984. Effective reflectance of oceanic whitecaps. Appl. Opt. 23, 1816–1824.

Lamquin, N., Clerc, S., Bourg, L., Donlon, C., 2020a. OLCI A/B tandem phase analysis, part 1: level-1 homogenisation and harmonisation. Remote Sens. 12, 1804. https://doi.org/10.3390/rs12111804.

Lamquin, N., Déru, A., Clerc, S., Bourg, L., Donlon, 2020b. C. OLCI A/B tandem phase analysis, part 2: benefits of sensors harmonisation for level-2 products. Remote Sens. 12, 2702. https://doi.org/10.3390/rs12172702.

Lohrenz, S.E., Cai, W.J., 2006. Satellite ocean color assessment of air-sea fluxes of CO2 in a river-dominated coastal margin. Geophys. Res. Lett. 33, 1–4. https://doi.org/10.1029/2005GL023942.

Maritorena, S., D'Andon, Hembise Fanton, Mangin, A., Siegel, D.A., 2010. Merged satellite ocean color data products using a bio-optical model: characteristics, benefits and issues. Remote Sens. Environ. 114, 1791–1804. https://doi.org/10.1016/j.rse.2010.04.002.

McClain, C.R., 2009. A decade of satellite ocean color observations. Annu. Rev. Mar. Sci. 1, 19–42. https://doi.org/10.1146/annurev.marine.010908.163650.

Mélin, F., Zibordi, G., Carlund, T., Holben, B.N., Stefan, S., 2013. Validation of SeaWiFS and MODIS Aqua/Terra aerosol products in coastal regions of European marginal seas. Oceanologia 55, 27–51. https://doi.org/10.5697/oc.55-1.027.

Mobley, C.D., Werdell, J., Franz, B., Ahmad, Z., Bailey, S., 2016. Atmospheric correction for satellite ocean color radiometry. In: NASA/TM-2016-217551, Goddard Sapce Flight Center, Greenbelt, USA, 73 pp.

Morel, A., Antoine, D., Gentili, B., 2002. Bidirectional reflectance of oceanic waters: accounting for Raman emission and varying particle scattering phase function. Appl. Opt. 41, 6289–6306.

Moulin, C., Gordon, H.R., Banzon, V.F., Evans, R.H., 2001. Assessment of Saharan dust absorption in the visible from SeaWiFS imagery. Geophys. Res. Lett. 106D (18), 239–249.

Nobileau, D., Antoine, D., 2005. Detection of blue-absorbing aerosols using near infrared and visible (ocean color) remote sensing observations. Remote Sens. Environ. 95, 368–387.

Ohring, G., Wielicki, B., Spencer, R., Emery, B., Datla, R., 2005. Satellite instrument calibration for measuring global climate change: report of a workshop. Bull. Am. Meteorol. Soc. 1303–1313. https://doi.org/10.1175/BAMS-86-9-1303.

Schueler, C.F., Clement, J.E., Ardanuy, P.E., Welsch, C., DeLuccia, F., Swenson, H., 2002. NPOESS VIIRS sensor design overview. In: Barnes, W.L. (Ed.), Earth Observing Systems VI. SPIE, pp. 11–23. https://doi.org/10.1117/12.453451.

Shettle, E.P., Fenn, R.W., 1979. Models for the aerosols of the lower atmosphere and the effects of humidity variations on their optical properties. Environmental Research Papers, AFGL-TR-79-0214, 20 September 1979, AFGL, Hanscom (Mass.).

Stramska, M., Petelski, T., 2003. Observations of oceanic whitecaps in the north polar waters of the Atlantic. J. Geophys. Res. Ocean. 108 https://doi.org/10.1029/2002jc001321.

Thuillier, G., Hersé, M., Labs, D., Foujols, T., Peetermans, W., Gillotay, D., Simon, P.C., Mandel, H., 2003. The solar spectral irradiance from 200 to 2400 nm as measured by the SOLSPEC spectrometer from the ATLAS and EURECA missions. Sol. Phys. 214, 1–22. https://doi.org/10.1023/A:1024048429145.

World Meteorological Organization (WMO), 2011. Systematic observation requirements for satellite-based data products for climate 2011. Update supplemental details to the satellite-based component of the implementation plan for the global observing system for climate in support of the UNFCCC (2010 update). Report GCOS —154. WorldMeteorological Organization.

Zibordi, G., Berthon, J.-F., Mélin, F., D'Alimonte, D., Kaitala, S., 2009a. Validation of satellite ocean color primary products at optically complex coastal sites: Northern Adriatic Sea, Northern Baltic Proper and Gulf of Finland. Remote Sens. Environ. 113, 2574–2591. https://doi.org/10.1016/j.rse.2009.07.013.

Zibordi, G., Holben, B., Slutsker, I., Giles, D., D'Alimonte, D., Mélin, F., Berthon, J.-F., Vandemark, D., Feng, H., Schuster, G., Fabbri, B.E., Kaitala, S., Seppälä, J., 2009b. AERONET-OC: A network for the validation of ocean color primary products. J. Atmos. Ocean. Technol. 26, 1634–1651. https://doi.org/10.1175/2009JTECHO654.1.

Zibordi, G., Holben, B.N., Talone, M., D'Alimonte, D., Slutsker, I., Ggiles, D.M., Sorokin, M.G., 2021. Advances in the Ocean Color Component of the Aerosol Robotic

Network (AERONET-OC). J. Atmos. Ocean. Technol. 38, 725–746. https://doi.org/10.1175/JTECH-D-20-0085.1.

Zibordi, G., Mélin, F., Voss, K.J., Johnson, B.C., Franz, B.A., Kwiatkowska, E., Huot, J.-P., Wang, M., Antoine, D., 2015. System vicarious calibration for ocean color climate change applications: Requirements for in situ data. Remote Sens. Environ. 159, 361–369.

Zibordi, G., Mélin, F., Berthon, J.-F., 2018. A regional assessment of OLCI data products. IEEE Geosci. Remote Sens. Lett. 15, 1490–1494. https://doi.org/10.1109/LGRS.2018.2849329.

Zibordi, G., Talone, M., Mélin, F., Sciuto, P., Berthon, J.-F., Bulgarelli, B., Canuti, E., 2019. Assessment of Copernicus OLCI Ocean Colour Data, EUR 29973 EN. Publications Office of the European Union, Luxembourg. https://doi.org/10.2760/41229. ISBN 978-92-76-13039-0. JRC118718.

Zibordi, G., Talone, M., Mélin, F., 2022. Uncertainty Estimate of Satellite Derived Normalized Water-Leaving Radiance. IEEE Geosci. Remote Sens. Lett. 19, 1–5. https://doi.org/10.1109/LGRS.2021.3134876.

Zibordi, G., Voss, K.J., 2014. Requirements and strategies for in situ radiometry in support of satellite ocean color. In: Experimental Methods in the Physical Sciences, 47. Academic Press, pp. 531–556.

Web references

Antoine, D., 2010. OLCI Level-2 Algorithm Theoretical Basis Document – Atmospheric Corrections over Case 1 Waters. Report S3-L2-SD-03- C07-LOV-ATBD. https://www.eumetsat.int/media/38630.

EUMETSAT, 2019. Recommendations for Sentinel-3 OLCI Ocean Colour product validations in comparison with *in situ* measurements – Matchup Protocols. UM/SEN3/DOC/19/1092968. https://www.eumetsat.int/media/44087 (last accessed on November 24, 2021).

EUMETSAT, 2021a. Sentinel-3 OLCI L2 report for Baseline Collection OL_L2M_003. EUM/RSP/REP/21/1211386. https://www.eumetsat.int/media/47794 (last accessed on November 24, 2021).

EUMETSAT, 2021b. Sentinel-3 OLCI Marine User Handbook. EUM/OPS-SEN3/MAN/17/907205. https://www.eumetsat.int/media/45743 (last accessed on November 24, 2021).

Fischer, J., Preusker, R., Lindstrot, R., 2010. OLCI Level-2 Algorithm Theoretical Basis Document – Correction of the Impact of the Absorption of Atmospheric Gases. Report S3-L2-SD-03-C03-FUB-ATBD. https://www.eumetsat.int/media/40899 (last accessed on November 24, 2021).

Hieronymi, M., Mazeran, C., Steinmetz, F., 2021. Ocean Colour Bright Pixel Correction – Product Validation. EUM/18/BPC/PVR. https://www.eumetsat.int/media/48560 (last accessed on November 24, 2021).

Lavander, S., Kay, S., 2010. OLCI Level-2 Algorithm Theoretical Basis Document – Glint Correction. Report S3-L2-SD-03-C09-ARG-ATBD. https://www.eumetsat.int/media/38633 (last accessed on November 24, 2021).

Mazeran, C., Hieronymi, M., Steinmetz, F., 2021. Ocean Colour Bright Pixel Correction – Algorithm theoretical basis. EUM/18/BPC/ATBD. https://www.eumetsat.int/media/48559 (last accessed on November 24, 2021).

Mazeran, C., Ruescas, A., 2021. Ocean Colour System Vicarious Calibration Tool, EUM/19/SVCT/D2. https://www.eumetsat.int/media/47502 (last accessed on November 24, 2021).

NASA, 2021. Level 2 Ocean Color Flags. https://oceancolor.gsfc.nasa.gov/atbd/ocl2flags/ (last accessed on November 24, 2021).

Vincent, E., Muguet, I., 2010. OLCI Level-2 Algorithm Theoretical Basis Document – Instrumental Corrections. Report S3-L2-SD-03-C04-ACR-ATBD. https://www.eumetsat.int/media/38634 (last accessed on November 24, 2021).